HHS Public Access

Author manuscript

Sci Signal. Author manuscript; available in PMC 2020 March 03.

Published in final edited form as:

Sci Signal. ; 12(597): . doi:10.1126/scisignal.aat4128.

Structure-function guided modeling of chemokine-GPCR specificity for the chemokine XCL1 and its receptor XCR1

Jamie C. Fox[1], **Monica A. Thomas**[1], **Acacia F. Dishman**[1], **Olav Larsen**[2], **Takashi Nakayama**[3], **Osamu Yoshie**[4], **Mette Marie Rosenkilde**[2], **Brian F. Volkman**[1,*]

[1]Department of Biochemistry, Medical College of Wisconsin, Milwaukee, WI 53226, USA.

[2]Department of Neuroscience and Pharmacology, University of Copenhagen, Copenhagen DK-2200, Denmark.

[3]Divison of Chemotherapy, Kindai University Faculty of Pharmacy, Higashi-osaka 577, Japan.

[4]The Health and Kampo Institute, 1-11-10 Murasakiyama, Sendai, Miyagi 982-3205, Japan.

Abstract

Chemokines interact with their G protein-coupled receptors (GPCRs) through a two-step, two-site mechanism and, through this interaction, mediate a wide array of homeostatic and immune response mechanisms. Upon initial recognition of the chemokine by the receptor, the N-terminus of the chemokine inserts into the orthosteric pocket of the GPCR causing conformational changes that trigger an intracellular signaling cascade. There is considerable structural and functional evidence to suggest that the amino acid composition and length of the chemokine N-terminus is critical for GPCR activation, complementing the size and amino acid composition of the orthosteric pocket. However, very few structures of a native chemokine-receptor complex have been solved. Here, we used a powerful hybrid approach that combines structure-function data with Rosetta modeling to describe key contacts within a chemokine-GPCR interface. We found that extreme N-terminal residues of the chemokine XCL1 (Val^1, Gly^2, Ser^3, and Glu^4) contribute a large fraction of the binding energy to its receptor XCR1, while residues near the disulfide bond-forming Cys^{11} residue modulate XCR1 activation. Alterations in the XCL1 N-terminus changed

*Corresponding author. bvolkman@mcw.edu.

Author contributions: JCF and BFV conceived and planned experiments. JCF produced and purified proteins, performed cell-based assays, analyzed data, and wrote the manuscript. MAT performed the computational modeling, analyzed modeling data, and assisted in manuscript writing and revision. OL performed cell-based assays, analyzed results, and assisted in manuscript revision. TN performed cell-based assays, analyzed results, and assisted in manuscript revision. AFD produced and purified protein, assisted MAT with computational modeling, and assisted with preparation of manuscript figures and manuscript revision. OY, MMR, and BFV provided financial assistance and support for all experiments represented in this manuscript and assisted in manuscript revision.

Competing interests: B.F.V. has ownership interests in Protein Foundry, LLC. All other authors declare that they have no competing interests.

Data and materials availability: All data needed to evaluate the conclusions in the paper are present in the paper or the Supplementary Materials.

Supplementary Materials

Fig. S1. Homology modeling of XCR1.

Fig. S2. 1 μs MD simulations of the XCR1-$XCL1^{N\text{-terminal peptide}}$ complex.

Fig. S3. MD simulations reveal Glu^4 interactions with $Tyr^{45.52}$.

Fig. S4. ^{125}I-XCL1 CC3 displacement and ^{3}H-IP_3 accumulation by XCR1 R6.62A.

Table S1. Summary of quantitative values from nonlinear regression for each XCL1 N-terminal variant.

Table S2. Summary of quantitative values for cellular migration and docking analysis.

XCR1 activation, as measured by inositol triphosphate accumulation, intracellular calcium release, and directed cell migration. Computational analysis of XCL1-XCR1 interactions revealed important functional contacts involving Glu^4 of XCL1 and Tyr^{117} and Arg^{273} of XCR1. Subsequent mutation of Tyr^{117} and Arg^{273} lead to diminished binding and activation of XCR1 by XCL1 in in vitro assays. These findings demonstrate the utility of a hybrid approach, using biological data and homology modeling, to study chemokine-GPCR interactions.

Introduction

The chemokine family consists of ~50 ligands and ~20 corresponding G protein-coupled receptors (GPCRs). Promiscuity, the ability of one chemokine to interact with multiple GPCRs and vice versa, is abundant in the chemokine network. Despite this promiscuity, chemokines mediate an extraordinarily specific and diverse array of homeostatic, inflammatory, and pathologic functions. This study focuses on understanding the interactions between the X-C motif chemokine ligand 1 (XCL1) and its cognate GPCR, XCR1. The XCL1-XCR1 axis is a major facilitator of dendritic cell (DC) and T-cell immune responses throughout the body. For example, mice lacking either XCL1 or XCR1 have a diminished $CD8^+$ T-cell response and lack the ability to generate T regulatory cells. This not only affects the T-cell population in the thymus (1), but also influences T-cell populations in the intestines of mouse models of colitis (2). The XCL1-XCR1 axis has been explored as a venue to enhance the efficacy of various cancer treatments, including anti-tumor vaccines (3–10), cancer gene therapies (11–13) and combined gene and adoptive T-cell therapies for cancers (14–16). These treatments have been proposed for a wide variety of cancers including myeloma (9, 16), B16 melanoma (3, 7, 8, 13), 3LL lung carcinoma (5, 8), breast cancer (11, 17), neuroblastoma (4, 10), lymphoma (14, 15), hepatocellular carcinoma (6), and colon carcinoma (12). As the immunological role and therapeutic potential of the XCL1-XCR1 axis continues to emerge, a detailed understanding of the key components that mediate XCL1-XCR1 binding and activation will enhance our ability to design XCL1-based therapeutics ranging from prophylactic vaccines to cancer treatments.

Chemokines engage their cognate GPCRs through a two-step, two-site binding mechanism of recognition and response (18–21). Like a nametag, the core of the chemokine bears an epitope that is recognized by the receptor N-terminus (site 1). Once identity has been confirmed, information is passed from the ligand to the receptor through insertion of the flexible N-terminal domain of the chemokine ligand into the orthosteric pocket of the GPCR (site 2). The orthosteric pocket is defined as the main ligand-binding pocket, and for chemokine GPCRs this binding site is typically located within the transmembrane domain of the receptor (22). Residues of the chemokine N-terminus make specific contacts within the orthosteric site that induce conformational changes and ultimately lead to a cellular response (step 2) (21) (Fig. 1). In addition to cytoskeletal remodeling and cellular migration, these pathways also signal for receptor desensitization and GPCR internalization (23). Under normal circumstances the process of receptor binding, activation, and desensitization is highly controlled. When this control is lost, aberrant chemokine signaling can contribute to a number of pathological conditions including autoimmune disease (24) and cancer progression (25).

In this study, we conducted a detailed structure-function and computational analysis of the site 2 interactions between XCL1 and XCR1. Unlike other chemokine family members, XCL1 exists in a unique, dynamic equilibrium between two native state conformations under near physiological conditions (26–28). One state is monomeric and retains the canonical chemokine fold. This state binds and activates XCR1 and does not bind to glycosaminoglycans (GAGs) (29). The second state is an atypical β-sandwich dimer that does interact with GAGs and establishes chemotactic gradients while not activating XCR1 (28). Descriptions of these extreme dynamic fluctuations are uncommon in structural biology, and proteins like XCL1 that exhibit similar behaviors are classified as metamorphic (30). Several studies demonstrate that the metamorphic behavior of XCL1 plays an important role in its biological activity. For example, the alternative XCL1 dimer conformation inhibits HIV infection in peripheral blood mononuclear cells, but the monomeric chemokine fold does not (31–33).

Using an engineered XCL1 monomer that retains full XCR1 agonist activity but is locked into the monomeric chemokine fold (29), we conducted alanine-scanning site-directed mutagenesis on the 10 N-terminal amino acids of XCL1 to identify key residues important for binding and activation of XCR1 (site 2). After measuring the receptor binding of each variant, we then conducted several assays to capture discrete signaling events and measured the ability of each XCL1 variant to activate XCR1. Finally, in conjunction with the aforementioned experimental approaches, we used computational modeling, docking, and molecular dynamics simulations to generate a model of the XCL1-XCR1 site 2 interactions. We then validated a subset of these computationally defined interactions in vitro through binding and signaling assays. Together with our previous work mapping its GAG binding site (34), our findings define the functional roles for a number of XCL1 residues. This analysis also demonstrates the utility of using a combined in vitro and in silico approach to study chemokine-GPCR interactions.

Results

Amino acids substitutions in the XCL1 N-terminus result in diminished XCR1 binding

Our initial attempts to develop a radioligand binding assay using ^{125}I-labeled wild-type (WT)-XCL1 were unsuccessful due to high levels of non-specific binding. We speculated that the metamorphic native state of XCL1 was the cause and overcame this limitation by using an engineered variant of XCL1 that prevents metamorphic interconversion. This variant, XCL1 CC3, contains two substitutions (V21C and V59C) that form a second disulfide bond which locks the protein into the monomeric chemokine fold (29). Our previous work demonstrated that XCL1 CC3 was slightly more potent than XCL1 WT as XCR1 agonist in an intracellular Ca^{2+}-flux assay (29). A recent study demonstrated that a murine version of XCL1 CC3 is a more potent XCR1 agonist in vitro than is WT mXCL1 and is more effective in vivo as an adjuvant for the induction of antigen-specific effector $CD8^+$ T cells (35).

First, radioligand displacement assays were used to measure the ability of each XCL1 N-terminal variant to displace ^{125}I-XCL1 CC3 possessing the native N-terminus. XCL1 WT was included in all analyses for comparison. COS-7 cells transfected with human XCR1

were treated with ^{125}I-XCL1 CC3 and various concentrations of XCL1 variants. XCL1 CC3 displaces ^{125}I-XCL1 CC3 with an EC_{50} of 1 nM (Fig. 2A and table S1). XCL1 WT had a seven-fold decreased affinity (EC_{50} = 7.7 nM), which may be due to its metamorphic conversion to the dimer form, thus lowering agonist concentrations and leading to weaker potency. The XCL1 CC3 variants, V1A, G2A, S3A, and E4A had decreased affinities ranging from 30 to 375 fold. G2A and E4A variants had the lowest affinity. Mutations that remove the N-terminal valine (ΔVal^1) or add an additional glycine on the extreme N-terminus ($+Gly^{N\text{-}term}$) also showed decreased affinities of > 100-fold. With the exception of V5A and K8A (EC_{50} = 8.0 nM and 5.2 nM, respectively), mutant residues S6A and R9A had increased affinity for XCR1 binding (EC_{50} values < 1.0 nM). The EC_{50} values for D7A and T10A were not significantly different when compared to XCL1 CC3 (table S1). Overall, alterations to residues 1–5 showed larger changes in binding affinity than did residues 6–10 (Fig. 2A).

Alteration of XCL1 N-terminal residues 1–5 disrupt inositol triphosphate (IP_3) accumulation

IP_3 accumulation assays are a common approach used to study chemokine receptor and G protein activation (36, 37). After chemokine binding and receptor activation, the G protein alpha (Gα) and beta-gamma (βγ) subunits dissociates from the intracellular face of the receptor. Depending on the type of GPCR, either the Gα or the βγ subunit then activates phospholipase-C (PLC) leading to cleavage of the membrane-bound phosphatidylinositol-4,5-bisphosphate (PIP_2) and the formation of IP_3 and diacylglycerol (DAG). For chemokine receptors, the βγ subunit is responsible for activation of PLC and formation of IP_3 (38). IP_3 functions as a secondary messenger by diffusing to the endoplasmic reticulum (ER) and mobilizing intracellular calcium stores that lead to a variety of intracellular signaling cascades (39) (Fig. 1).

XCL1 N-terminal variants were incubated with COS-7 cells transfected with XCR1 and Gqi4myr. Gqi4myr is an engineered chimeric $Gα_q$ protein containing several modifications that allow for $Gα_i$ receptors (i.e. chemokine receptors) to signal through the $Gα_q$ pathway and activate PLC. It is important to note that the majority of PLC is activated through the $Gα_q$ pathway when using the Gqi4myr system. However, it is likely that the endogenous βγ subunit, as mentioned above, may also activate PLC but to a lesser extent. XCL1 N-terminal variants were assayed for their ability to stimulate tritium (^{3}H)-IP_3 accumulation within the cell (Fig. 2B and table S1). XCL1 CC3 and WT had comparable IP_3 accumulation (EC_{50} = 14.1 nM and 17.6 nM, respectively), likely indicating that the metamorphic behavior of WT has a negligible effect on XCR1 activation in the context of the IP_3 accumulation assay. Consistent with radioligand-binding results, variant residues within the extreme N-terminus of XCL1 (V1A, G2A, S3A, E4A, V5A, ΔVal^1, and $+Gly^{N\text{-}term}$) displayed large defects in IP_3 accumulation with potency decreases of 2.8 to90 fold. IP_3 was below detectable levels in cells treated with G2A, and an EC_{50} could not be determined. E4A and ΔVal^1 had the largest decrease in potency (~ 90-fold). With the exception of S6A, all remaining variants proximal to Cys^{11} (D7A, K8A, R9A, and T10A) displayed IP_3 accumulation similar to CC3. It is likely that a correlation exists between receptor affinity of variants 1–5 and their ability to promote IP_3 accumulation. Conversely, mutations of residues 7, 8, 9, and 10 had a negligible effect on XCR1 activation, likely indicating that Asp^7, Lys^8, Arg^9, and Thr^{10} in the native

XCL1 sequence play a minimal role in XCL1-mediated XCR1 signaling response. Similar to the binding assay, S6A displayed a marked increase in potency (3-fold) for IP_3 accumulation when compared to XCL1 CC3. It is possible that Ser^6 may function to divide the extreme N-terminal residues (Val^1-Val^5) from the residues near the Cys^{11} (Asp7-Thr^{10}) and dampen XCL1-mediated XCR1 signaling response (table S1).

Several XCL1 N-terminal variants have decreased potency for intracellular calcium flux

Accumulated IP_3 triggers the release of calcium from the ER causing a pulse in intracellular calcium release, which can be measured by a calcium flux assay (Fig. 1). Like IP_3 accumulation, intracellular calcium flux is another second messenger and reporter of GPCR activation, allowing for measurement of ligand potency (40). Potency describes the concentration of XCL1 ligand needed to produce a calcium flux response and is quantified by EC_{50}, while efficacy describes the maximal calcium flux response achievable by an XCL1 ligand.

XCR1-expressing HEK293 cells were treated with various concentrations of XCL1 variants (Fig. 3A, table S1). XCL1 WT, and S6A have mildly decreased potencies (1.4-fold and 2.1-fold, respectively) and shared efficacies of ~80 relative fluorescent units (RFUs) for calcium flux when compared to CC3. The V5A, R9A and T10A variants also had similar decreased potencies (1.6 to 2.6-fold), however these variants display decreased efficacies of approximately two-fold (RFUs < 60). All other N-terminal variants (V1A, G2A, S3A, E4A, D7A, K8A, ΔVal^1 and $+Gly^{N\text{-term}}$) displayed reduced potencies of 6- to 93-fold (EC_{50} > 268 nM), with E4A and ΔVal^1 having the most reduced potencies of 93-, and 69-fold, respectively. The reduction in calcium release by D7A, K8A, R9A, and T10A does not correlate with the observed lack of effect of these variants in the IP_3 accumulation, indicating that responses to changes in the XCL1 agonist can vary between assay types (table S1).

Alterations of Val^1 - Glu^4 cause diminished cellular migration

The ability of a cell to respond and move toward a chemical stimulus is known as chemotaxis, and measurement of this phenomenon is a foundational tool for assessing chemokine function (41). Typically, cells exhibit a biphasic (bell-shaped) chemotactic response, dependent on chemokine concentration. This means that cellular migration increases with increasing chemokine concentration until a concentration threshold is reached. Upon reaching this threshold, the cell is unable to respond to the additional increases in chemokine concentration and migration is decreased (42).

L1.2 murine cells were transfected with human XCR1 and incubated in transwell plates with various concentrations of XCL1 variants (Fig. 3B, table S2). Maximal chemotaxis occurs at 1 nM for XCL1 CC3, S6A, D7A, K8A, R9A and T10A. XCL1 WT stimulated maximal chemotaxis at 10 nM, which was similar to V5A. The XCL1 variants that showed the largest defects in chemotactic migration were V1A, G2A, S3A, E4A, ΔVal^1 and $+Gly^{N\text{-term}}$, all having ~1,000-fold decrease in potency (maximal chemotaxis ≥ 1000 nM). Of these, G2A displayed the largest defect in chemotaxis stimulation (Fig. 3B). When correlating calcium flux EC_{50} for each variant with its maximal chemotaxis at 1 nM, variants S6A-T10A

retained levels of XCR1 activation similar to XCL1 CC3 while extreme N-terminal variants had the largest disruption in XCR1 activation (Fig. 3C).

Modeling of XCR1-XCL1 N-terminal Interactions

To better interpret the experimental data for XCR1 activation, we constructed a structural model of the site 2 interactions between the N-terminus of XCL1 and the orthosteric pocket (i.e., the main ligand binding pocket) of XCR1. For chemokine receptors this site is comprised of molecular contributions from transmembrane regions III-VII (major binding pocket) and transmembrane I-III and VII (minor binding pocket) (43). As an experimentally determined structure of XCR1 has not yet been published, we began our efforts by generating a homology model of XCR1 using the comparative modeling protocol of Rosetta (RosettaCM) (44, 45). The benefit of this technique for creating a homology model of XCR1 is that it utilizes multiple template structures instead of a single homolog, leading to the generation of more accurate models than other currently available methods (45). The generated XCR1 model has a favorable energy score and was found to be stable over the course of a 300 ns all-atom molecular dynamics (MD) simulation (average Cα root mean square deviation (RMSD) = 3.2 Å; fig. S1, A and B) indicating stable intramolecular interactions. Because we wanted to dock the N-terminal peptide of the chemokine into the orthosteric pocket, we chose three models of XCR1, which were selected by visual inspection from frames across the MD trajectory in which the orthosteric pocket was allowed to relax from a relatively closed conformation to become more accessible to a chemokine ligand. The N-terminal peptide of XCL1 (Val^{1}-Gly^{2}-Ser^{3}-Glu^{4}-Val^{5}-Ser^{6}-Asp^{7}-Lys^{8}-Arg^{9}-Thr^{10}) was docked using Rosetta's FlexPepDock ab initio protocol (46). For each XCR1 starting pose, 100,000 models were generated in the first round of unbiased docking. 3–5% of these models docked to the orthosteric pocket of XCR1, as chosen by a cutoff distance of < 10 Å between Val^{1} and $Trp^{2.60}$ (Ballesteros-Weinstein nomenclature, used here and throughout for numbering GPCR residues, is a scheme in which the first number denotes the transmembrane helix, and the second number denotes relative position with respect to the most conserved residue in each helix, which is assigned number 50). As mutation of Glu^{4} to alanine resulted in a severe disruption of XCL1-XCR1 binding and activation in vitro (tables S1 and S2, Fig. 4, A to C), the energy contribution of Glu^{4} was used to select models in which Glu^{4} was making a favorable interaction (meaning, a negative energy contribution). Models that adhered to the aforementioned distance and energy requirements were clustered and a single representative model was selected for each XCR1 starting pose. These models were each used to seed the generation of an additional 100,000 docked models. Of these 100,000 re-docked models, ~90% docked to the orthosteric pocket of XCR1. Models were again filtered and clustered as above, and a single structure was selected for further analysis. The final model selection was based on agreement of in vitro data (Fig. 4, A to C) with the results of a computational alanine scan performed in the Robetta online server (47, 48). During the computational alanine scan, each non-glycine residue of the N-terminus of XCL1 was individually mutated to alanine. and the change in binding energy (ddG) was calculated (Fig. 4, D, table S2). When compared to the experimental EC_{50} values obtained from radioligand displacement, calcium mobilization, and IP_3 accumulation assays (Fig. 4, A to C, table S1), the ddG values calculated by Robetta for the selected pose showed agreement at critical residues, including Glu^{4} (Fig. 4D). The

ddG value for the G2A substitution was not calculated as the energy function utilized by the Robetta server requires alanine to be smaller than the residue it is replacing (47). Thus, our computational alanine scan could not predict the large loss of binding affinity seen experimentally with the G2A substitution. Additionally, the computational alanine scan incorrectly predicted a large loss for the S6A variant (Fig. 4, A to D). These data contributed to a selected XCR1-XCL1$^{\text{N-terminal peptide}}$ model (Fig. 4E).

To further analyze the contact stability of the selected pose, we performed four 1 μs all-atom molecular dynamics simulations on the XCR1-XCL1$^{\text{N-terminal peptide}}$ complex (fig. S2). When calculating RMSDs for our simulations, superpositioning was performed using the R package Bio3D, with the first frame of the MD simulation used as the reference coordinate set and the coordinates from the rest of the MD simulation used as the mobile dataset (a single representative simulation is shown in Fig. 4 for clarity). Over the course of the four 1 μs simulations, the peptide remained in the orthosteric pocket of the receptor, with an average C-alpha RMSD of <5 Å for the first four residues of the peptide (Fig. 4, F and G, and fig. S2A). Whereas the first five residues appear to make substantial contacts that enable low RMSD of the backbone over the course of the simulation, the last five residues make significantly fewer contacts and have a much larger Cα RMSD distribution (Fig. 4, F and G, and fig. S2A).

To gain a more global sense of the molecular contacts made in our modeled XCR1-XCL1$^{\text{N-terminal peptide}}$ complexes, the top scoring 100 docked models from each XCR1 starting pose were analyzed for their molecular contacts (Fig. 4H). Despite that each of the three initial XCR1 poses was randomly selected from the MD simulation trajectory, the complexes generated from all three starting poses share contacts with XCR1 residues known to make contacts in other chemokine-chemokine receptor complexes, including contacts with Trp$^{2.60}$ and Asn$^{3.29}$ (Fig. 4H).

Returning to our single selected model, visual inspection of the docked pose was performed with a focus on residues that caused large changes in the signaling ability of XCL1 in vitro. This revealed key XCR1-Val^{1} and XCR1-Glu^{4} intermolecular contacts. Specifically, important contacts were seen between the side chain Val^{1} and the side chains of Tyr$^{45.52}$, Trp$^{5.35}$, Phe$^{3.32}$, as well as potential hydrogen bond interactions between the amino terminus of Val^{1} and His$^{4.64}$ and Asn$^{3.29}$ (Fig. 4I), implicating these residues as key mediators of the XCL1-XCR1 interaction. Visual inspection also revealed three important contacts for Glu^{4}. A potential hydrogen bond interaction between Glu^{4} and Arg$^{6.62}$ and Tyr$^{45.52}$ (Fig. 4J) provides a possible explanation for the large binding and activation defect seen experimentally for the XCL1 E4A variant (Fig. 4, A to C). Though not within a hydrogen bonding distance of Arg$^{7.39}$ in the selected model, Glu^{4} is within 5 Å of Arg$^{7.39}$, and thus we identified Arg$^{7.39}$ as a third residue that may also be important for Glu^{4}-mediated XCL1-XCR1 interactions. Furthermore, position 7.39 is highly conserved among chemokine receptors as a negatively charged glutamate (49), suggesting the positively charged Arg$^{7.39}$ may be mediating the interaction specific between XCR1 and XCL1.

In the context of our experimental data, we find agreement between the in silico and in vitro results in that both indicate the importance of the Val^{1}, Gly^{2}, Ser^{3}, and Glu^{4} in the XCL1-

XCR1 site 2 interaction. Additionally, the experimental and computational data suggest that Ser^{6}, Asp^{7}, Lys^{8}, Arg^{9}, and Thr^{10} act as a linker between the core of XCL1 and the site 2 interaction, providing the length necessary for XCL1 to fully bind to and activate XCR1.

Molecular Dynamics Simulations Predict Key Interactions of the Amino Terminus of XCL1 with $Asp^{4.60}$ and $Asn^{3.29}$

As truncation (ΔVal^{1}) or extension ($+Gly^{N\text{-term}}$) of the amino terminus of XCL1 drastically alters XCL1 binding to and activation of XCR1 (table S1), we further investigated which XCR1 residues were making important contacts with Val^{1} by analyzing the relative position of Val^{1} over the course of four 1 μs molecular dynamics simulations. We analyzed the interactions made between the amino terminus of the $XCL1^{N\text{-terminal peptide}}$ and XCR1 over the course four 1 μs all-atom molecular dynamics simulations (Fig. 5, fig. S2B). The MD simulations allowed for capture of additional binding contacts that were not previously identified in our initial Rosetta-generated XCR1-$XCL1^{N\text{-terminal peptide}}$ complexes, due in part to differences in the Rosetta energy function and the Chemistry at HARvard Macromolecular Mechanics (CHARMM)forcefield. We found the amino terminus of the $XCL1^{N\text{-terminal peptide}}$ primarily interacts with three residues: $Asn^{3.29}$, $His^{4.64}$, and $Asp^{4.60}$ (Fig. 5A). In the selected Rosetta model, the amino terminus of the $XCL1^{N\text{-terminal peptide}}$ is making hydrogen bond contacts with $His^{4.64}$ and $Asn^{3.29}$, but the MD simulations revealed an additional possible interaction as the amino terminus of the $XCL1^{N\text{-terminal peptide}}$ moved within hydrogen bonding distance of $Asn^{3.29}$ and $Asp^{4.60}$ (Fig. 5, B to D, and fig. S2B). Although positions 3.29 and 4.60 have been identified as contacts in previously crystalized ligand-chemokine receptor complexes (50), neither position is highly conserved, though a negatively charged residue is common at position 4.60 (Fig. 5E). Because it is already known that the distal N-termini of chemokines commonly interact with the orthosteric pockets of their respective chemokine receptors (50), we did not focus our efforts on in vitro validation of XCL1 Val^{1} receptor contacts, but rather on XCL1 Glu^{4} receptor contacts, which we expect to be more important for enhancing XCL1-XCR1 specificity of binding.

Modeling dynamics simulation predicts key interaction of XCL1 Glu^{4} with $Arg^{6.62}$, $Arg^{7.39}$, and $Tyr^{45.52}$ of XCR1

As Glu^{4} of XCL1 was shown to be critical for binding and activation of XCR1 by ^{125}I-displacement, IP_3 accumulation, calcium flux, and chemotaxis assays, we sought to determine the XCR1 contacts that might be mediating this critical interaction. Analysis of the intermolecular contacts (i.e., atom-atom distances < 3 Å) between Glu^{4} and XCR1 in the top 100 models for each XCR1 pose (Fig. 4H) revealed that Glu^{4} may interact with residues in transmembrane domains VI and VII as well as residues within ECL2. However, the most frequent Glu^{4} contact observed in our modeling was with $Arg^{6.62}$ (Fig. 4H). Thus, further investigation of Glu^{4}-XCR1 interactions was performed through analysis of the relative position of the Glu^{4} side chain over the course of the aforementioned four 1 μs molecular dynamics simulations. During the simulations, Glu^{4} interacts with $Arg^{6.62}$, $Arg^{7.39}$, and $Tyr^{45.52}$ (Fig. 6, A to C, and fig. S3, A to C). The Glu^{4}-$Arg^{7.39}$ is particularly interesting given the significance of position 7.39 for chemokine receptors (51). In nearly all other chemokine receptors, residue position 7.39 is a glutamate and is thought to make important contacts with the chemokine ligand (52) (Fig. 6D). Indeed, in the three currently published

crystal structures of chemokine-receptor complexes, the chemokine N-terminus makes important contacts with residue 7.39 (53–55). Of all chemokine receptors, only XCR1 and CCRL2 have positively charged residues at positions 7.39. Given the significance of Glu^{4} in the N-terminus of XCL1 and the potential for a Glu^{4}-$Arg^{7.39}$ interaction shown via molecular dynamics simulations (Fig. 6, E and F, and fig. S2C), we propose that transient interactions between Glu^{4} (XCL1) and $Arg^{7.39}$ (XCR1) are important for binding and stabilization of the N-terminus of XCL1 in the orthosteric pocket of XCR1. Additionally, the molecular dynamics simulation further suggested a possible interaction between Glu^{4} in the N-terminus of XCL1 and $Tyr^{45.52}$ in ECL2 of XCR1 (Fig. 6, E and F, and figs. S2C and S3, A to C). However, this position is not highly conserved amongst chemokine receptors (fig. S3D).

Alteration of XCR1 residues $Arg^{7.39}$ and $Tyr^{45.52}$ result in diminished XCL1 binding and accumulation of IP_3

To test the importance of XCR1 residues $Arg^{6.62}$, $Arg^{7.39}$, and $Tyr^{45.52}$ for XCL1 binding and signaling, each of these residues were mutated to alanine, and binding and signaling assays were performed. The ability of XCL1 CC3 to displace ^{125}I-XCL1 CC3 from XCR1 variants was measured using radioligand displacement assays. XCR1 WT was used as a positive control. These assays were performed as described earlier in the results section. As compared with XCR1 WT (Fig. 6G), XCR1 R7.39A and XCR1 Y45.52A showed major defects in their ability to bind XCL1 CC3 (Fig. 6, H and I). XCR1 R6.62A was able to bind CC3 with an affinity similar to that of WT XCR1 (fig. S4). This demonstrates that XCR1 residues $Arg^{7.39}$ and $Tyr^{45.52}$ are critical in facilitating XCR1 binding to XCL1. IP_3 accumulation in response to treatment of cells expressing XCR1 variants with XCL1 CC3 was measured. XCR1 R7.39A and XCR1 Y45.52A, but not XCR1 R6.62A, display large defects in IP_3 accumulation (Fig. 6, J to L, and fig. S4), consistent with radioligand-binding assays. In all, these results support the conclusion drawn from our computational modeling that binding and signaling at the XCL1-XCR1 axis critically depends on XCR1 residues $Arg^{7.39}$ and $Tyr^{45.52}$. Broadly, this demonstrates the utility of a hybrid approach including both in vitro and in silico components to better understand ligand-receptor interfaces.

Discussion

Mutagenic studies of chemokines including CCL5 (56), CXCL8 (57), and CXCL12 (58) have shown that amino acid composition in the N-terminus is important for receptor binding and activation. With the exception of some CXC chemokines that harbor an N-terminal Glu-Leu-Arg (ELR) motif (59), there is little consensus among chemokine N-termini. Because chemokines orchestrate a large variety of homeostatic and pathologic functions, knowledge of the structural features that encode chemokine-receptor specificity is important for understanding immune function and developing new therapeutic strategies. In this study we combined structure function studies of XCL1 with computational modeling to identify key residues within the chemokine N-terminus that mediate binding and activation of XCR1. A panel of N-terminal XCL1 variants (V1A, G2A, S3A, E4A, V5A, S6A, D7A, K8A, R9A, and T10A) including an N-terminal truncation (ΔVal^{1}) and extension ($+Gly^{N\text{-}term}$) was analyzed using cell-based assays (radioligand displacement, IP_3 accumulation, calcium flux,

and chemotaxis) and computational analysis (modeling, docking, and molecular dynamics simulations). The results define several key interactions between the N-terminus of XCL1 and XCR1.

N-terminal substitutions (Val^1, Gly^2, Ser^3, and Glu^4), as well as amino-terminus modifications (ΔVal^1 and $+Gly^{N\text{-}term}$), introduce substantial defects in XCR1 binding suggesting that both the length and amino acid composition of the XCL1 N-terminus are crucial. These results are supported by computational modeling analysis. Docking and MD simulations show that alterations of Val^1 through mutation (V1A), deletion (ΔVal^1), or extension ($+G_{N\text{-}term}$) likely prohibit interactions between the XCL1 N-terminus and residues lining the bottom of the orthosteric pocket of XCR1. These XCR1 residues, found within the transmembrane helices (TM), include $Trp^{2.60}$ (TM2), $His^{4.64}$ (TM4), $Trp^{5.35}$ (TM5), and most likely serve as an anchoring point for the N-terminus of XCL1 in the orthosteric pocket. Removal or alternation of Val^1 prohibits anchoring and diminishes XCL1-XCR1 binding. This finding is consistent with previous studies that have shown that changes or truncations of the extreme amino-terminus of chemokines result in altered receptor binding and activation (20, 60).

Two additional residues in the N-terminus of XCL1, Gly^2 and Glu^4, mediate specific contacts with residues of XCR1. The G2A and E4A mutations lead to > 100-fold decrease in XCR1 binding affinity when compared to XCL1 CC3 in radioligand displacement assays. E4A displayed the largest change in binding energies (ddg > 1) according to docking analysis, while the ddg calculation was not able to predict the large loss of binding affinity caused by the G2A variant. Molecular Dynamics (MD) simulations further support contributions of Glu^4 in XCR1 binding, illustrating a primary interaction with $Arg^{6.62}$ and $Tyr^{45.52}$ and a secondary interaction with $Arg^{7.39}$. Inspection of chemokine receptor homologs at the 6.62, 7.39, and 45.52 positions revealed a majority of chemokine receptors have a $Glu^{7.39}$ (49), whereas there is no consensus for 6.62 or 45.52. Previous studies have shown that position 7.39 in other chemokine receptors make important contacts with chemokine N-termini, illustrating the importance of this position in chemokine-receptor interactions (50, 53–55). Previous works have also shown that in several GPCRs, both in the chemokine family and in other receptor families, position 45.52 makes key contacts with ligands (61). For example, receptor position 45.52 has been shown to make key contacts in the chemokine receptor-ligand complexes US28-CXC_3CL1, US28-vMIP-II, and CXCR4-CVX15 (50). Additionally, position 45.52 in rhodopsin interacts with rhodopsin ligand retinal (62), and position 45.52 in the 5-HT_{2A} receptor interacts with the antipsychotics zotepine and pimavanserin (63). In all, this demonstrates the significance of position 45.52 in GPCR-ligand interactions including but not limited to interaction between chemokine receptors and their ligands. The Glu^4 carboxylate of XCL1 likely interacts with $Arg^{6.62}$, $Arg^{7.39}$, and $Tyr^{45.52}$. due to their close proximity in the XCR1 orthosteric pocket. Upon mutation of Glu^4 to alanine, binding energy analysis reveals a large variation in ddg (>1). Ser^3 and Val^5 may also contribute to XCR1 binding according to our analysis but their impact is minimal in comparison to Gly^2 and Glu^4.

As expected, N-terminal variants that displayed defective XCR1 binding (Val^1, Gly^2, Ser^3, Glu^4, Val^5, ΔVal^1, and $+G^{N\text{-}term}$) also exhibit downstream defects in receptor activation as

measured through IP_3 accumulation, calcium flux, and cell migration assays. However, not all variants displayed defects in XCL1-XCR1 binding, such as those closest to Cys^{11} and distal from the extreme N-terminus: S6A, D7A, K8A, R9A, and T10A. According to ^{125}I-XCL1-CC3 displacement assays, these variants bound to XCR1 with affinities equal to or greater than XCL1 CC3 ($EC_{50} \leq 1.0$ nM). Both ^{125}I-XCL1-CC3 displacement assays and the MD simulation demonstrate that Ser^6, Asp^7, Lys^8, Arg^9, and Thr^{10} residues do not contribute to XCL1-XCR1 affinity. Specifically, the MD simulation illustrates that these residues are more dynamic, displaying more flexibility than the extreme N-terminal residues, suggesting they serve as a link to the folded XCL1 chemokine domain.

Mutation of Val^5, Ser^6, Asp^7 Lys^8, Arg^9 and Thr^{10} led to inconsistent effects on XCL1-mediated XCR1 responses in vitro (minimal effects on IP_3 accumulation and cellular migration, and larger effects in calcium response). The molecular dynamics simulation demonstrated enhanced flexibility of residues Ser^6-Thr^{10} within the orthosteric-binding pocket of XCR1. It is possible that dynamics within this region of the N-terminus may influence the ability of residues Ser^6-Thr^{10} to activate XCR1. These computational and biological findings warrant further examination (64).

It is important to note that no single mutation displayed antagonistic properties, meaning displayed tight binding without activation. This is consistent with the findings in a recent study by Kroczek *et al.* (65), showing that deletion of the seven N-terminal amino acids of murine diminished XCR1 binding by approximately 50-fold and lead to reduced chemotatic activity. These results indicate that multiple residues contribute to both receptor binding and activation. Previous studies have demonstrated that site 1 interactions, between the chemokine and the N-terminus of the cognate receptor, are important for initial chemokine-receptor binding (43). These contacts may also be major contributors to XCL1-XCR1 binding and contributions from both site 1 and 2 are needed for high affinity binding. Studies targeting the site 1 interaction between XCL1-XCR1 were not examined in this manuscript. In addition to XCL1, humans and several other species have a closely related paralog XCL2. XCL2 varies form XCL1 by two N-terminal amino acid changes (D7H and K8R). We have previously examined the ability of XCL2 to signal through XCR1, finding that XCL1 and XCL2 displayed similar activation profiles for calcium release and cellular migration (66). The structure-function analysis of the XCL1 N-terminus presented here is consistent with our previous findings that XCR1 activation is not particularly sensitive to the amino acids at positions 7 and 8.

In the absence of a solved structure of XCL1-XCR1, we have developed an in silico and in vitro approach to study both the functional and structural effects of XCL1-XCR1 site 2 binding. Homology modeling and MD simulations complemented the functional data and allowed us to visualize important contacts for XCR1 binding and activation including Glu^4 interactions with $Arg^{6.62}$, $Arg^{7.39}$, and $Tyr^{45.52}$ in XCR1. As a sequence comparison across the chemokine family revealed that most chemokine receptors possess a glutamate at position 7.39, and multiple studies have identified position 7.39 as an important mediator of ligand-receptor interactions (49, 50, 53–55), we have identified $Arg^{7.39}$ as being a unique residue that may be playing an important role in mediating XCL1-XCR1 interaction specificity. To probe the importance of XCR1 residues $Arg^{6.62}$, $Arg^{7.39}$, and $Tyr^{45.52}$,

binding and signaling assays were performed with XCR1 variants that altered these residues. XCR1 R7.39A and XCR1 Y45.52A showed significantly diminished binding to XCL1 CC3. Cells expressing these XCR1 variants also showed a major decrease in IP_3 accumulation in response to treatment with XCL1 CC3. XCR1 R6.62A exhibited binding and signaling capacity similar to that of WT XCR1. These data demonstrate that XCR1 residues $Arg^{7.39}$ and $Tyr^{45.52}$ are critical for XCL1-XCR1 binding and signaling. Moreover, these results support the utility of the computational modeling pipeline developed here, inspiring confidence in future application of these techniques to other chemokine-receptor pairs.

Additional studies measuring GPCR kinase (GRK) phosphorylation, β-arrestin recruitment, and receptor internalization are needed to better understand XCL1-XCR1 mediated signal transduction that drives dendritic cell chemotaxis. Herein, we have described a hybrid approach that combines experimental and in silico methods to characterize the chemokine-receptor interface of XCL1 and its GPCR XCR1. We propose that this strategy can be readily adapted for other members of the chemokine family to better interpret existing data or guide future functional studies.

Materials and Methods

Mutagenesis of XCL1 and XCR1 and purification of recombinant XCL1

QuikChange Site-directed mutagenesis kit (Agilent) was used to complete alanine-scanning mutagenesis of the N-terminal residues (1–10) of the locked-monomer conformation of XCL1 (CC3) that was previously described by Tunistra *et al* (29). Recombinant protein expression and purification was carried out as previously described (66). The molecular weights of all XCL1 purified proteins were verified by MALDI-TOF mass spectrometry. XCR1 variants were commercially provided by GenScript in the pcDNA3.1(+) vector, using the company's gene synthesis and mutagenesis services.

Molecular biology

The following methods were based on previously published methods (67). XCR1 cDNA was cloned into the pcDNA3.1(+) vector (Invitrogen) using sticky end ligation. XCR1 was amplified from this vector using PCR with end primers without a stop codon before insertion into the pCMV-ProLink™1 (PK1) vector (DiscoveRx, Birmingham, UK) directly upstream of the PK1 tag needed for the beta-arrestin2 recruitment assays. The product was transformed into XL1-Blue cells for monoclonal vector selection, and a purified vector product was sequenced before use.

In vitro mammalian cell culture

As previously described (67), COS-7 cells grown in Dulbecco's modified Eagle's medium 1885 (10% fetal bovine serum, 2mM Glutamine, 180 units/ml penicillin and 45 μg/ml streptomycin) at 37°C and 10% CO_2. Cells were transiently transfected with the pcDNA3.1(+) XCR1 vector using the calcium phosphate precipitation method and incubated for ~40 hours prior to performing assays.

Radioligand competition binding assay

Assay was performed as previously described (67). An XCL1 tracer was produced by iodine labeling of tyrosine residues of the XCL1 protein by employing an oxidative iodination procedure (using ChloramineT to incorporate a ^{125}I isotope (PerkinElmer), and the product was purified and verified by reverse-phase HPLC chromatography (68). COS-7 cells transfected with XCR1 were seeded in 96-well plates at 35,000 cells/well (in duplicates) for growth one day prior to the assay. On the day of the assay, the cells were washed and changed to a 50 mM HEPES buffer supplemented with BSA (5 g/l), and chilled to 5°C. Ligands were added shortly before the labeled XCL1 CC3 tracer (calibrated to result in ≈10% tracer binding), and the cells were incubated at 4°C for 3 hours before being washed in a 50 mM HEPES buffer containing BSA (5 g/l) and NaCl (29.22 g/l). The cells were lysed and gamma radiation of the lysate was measured.

Inositol triphosphate (IP_3) accumulation assay

Assay was performed as previously described (67). COS-7 cells were transfected with human XCR1 and G_{qi4myr}, a large G protein chimera with the $G\alpha_i$ recognition interface and a $G\alpha_q$ output. Cells were seeded into 96-well plates at 35,000 cells/well (in duplicates) one day before the assay, and incubated for growth with [^{3}H] myo-inositol (5 μL/mL, 2 μCi/mL) overnight. On the day of the assay, cells were washed in HBSS buffer, and changed to a solution of 10 mM LiCl in HBSS before ligands were added. After incubating for 90 minutes at 37°C, the cells were lysed in 10 mM formic acid, and 35 μl lysis solution (≈90 v/v%) was transferred to white and opaque 96-well plates and mixed with a solution of agitated SPA-Ysi beads (80 μl/well, 12.5 mg/ml, PerkinElmer). The plates were shaken for 30 minutes before being left for an 8-hour equilibration period, and finally scintillation was measured using a Packard Top Count NXT™ counter (PerkinElmer). Assays were conducted in triplicate.

Calcium flux assay

Calcium flux was measured in stable transfected XCR1-expressing HEK293 cells, generously provided by Dr. Joseph Hedrick (Schering-Plough Research Institute) (69), using a previously described method (66). Briefly, cell cultures were grown to ~90% confluency, lifted from the culture plate, washed 2x in warmed PBS, and suspended in assay buffer (1x HBSS, 20 mM HEPES (pH 7.4), and 0.1% BSA). Cells were plated at 2.0×10^5 cells/well in 100 μL in a 96-well plate and incubated with 100 μL of FLIPR Calcium 4 Assay Dye (Molecular Devices) for 1 h at 37 °C and 5% CO_2. A Flexstation 3 (Molecular Devices) was used to treat cells with various concentrations of purified proteins and monitor calcium flux. All experiments were conducted in triplicate.

Chemotaxis assay

Chemotaxis assays were carried out as previously described (66) using murine L1.2 cells stably expressing human XCR1 (70). In brief, 2.0×10^5 cells were suspended in 25 μL of assay media [phenol red free RPMI 1640, 0.5% BSA, and 10 mM HEPES (pH 7.4)] and added to the upper chambers of a transwell assay plate. XCL1 proteins were diluted to various concentrations in 30 μL of the same medium and added to the lower chambers. The

plates were incubated at 37 °C and 5% CO_2 for 1.5 hours. After incubation, cells that migrated into the lower wells were lysed with 0.1% Triton X-100 and measured by PicoGreen doubled-stranded DNA quantitation reagent (Molecular Probes). Assays were conducted in duplicate and the numbers of cells in the lower wells were expressed as a percentage of input cells. Results are shown as mean ± SEM for three separate experiments.

Homology Modeling

Homology modeling of XCR1 was performed using the RosettaCM protocol (44, 45). The human XCR1 sequence was obtained from UniProt (71) (UniProtKB Accession Number: P46094) and subsequently edited to remove both the N- (1-MESSGNPESTTFFYYDLQS-19) and C-terminal domains (304-QFWFCRLQAPSPASIPHSPGAFAYEGASFY-333). Seven template structures were chosen based on availability of structural information and sequence similarity to human XCR1: Human CCR5 (PDB ID: 4MBS), Human CXCR4 (PDB ID: 4RWS), Human CCR2 (PDB ID: 5T1A), Human CCR9 (PDB ID: 5LWE), Human Angiotensin II Receptor Type I (AT1R; PDB ID: 4YAY), Human Delta Opioid Receptor (δOR; PDB ID: 4RWA), and Murine Mu Opioid Receptor (μOR; PDB ID: 4DKL). The template structure PDBs were edited to remove any crystallographic inserts (e.g., T4 Lysozyme, Cytochrome B) and to remove the N- and C-terminal domains. The edited template PDBs were cleaned to remove extraneous information using the Rosetta script *clean_pdb.py*. Sequences were aligned to the edited XCR1 sequence using Clustal Omega (72), and the sequence alignment was manually adjusted to eliminate gaps in transmembrane (TM) regions and to align the conserved cysteine residue in extracellular loop 2 (ECL2). XCR1 fragments were generated using the Robetta server (73), and the TM topology of XCR1 was predicted using OCTOPUS (74). The aligned sequence of XCR1 was threaded onto each of the seven template structures, and the resultant threaded models were used to generate 5000 hybridized models using the hybridize mover of Rosetta scripts (44, 45). Each of the 5000 generated models was subjected to 2 all-atom sampling relaxation runs using Rosetta's relax application (75). The top 20 scoring models were visually inspected, and one model was selected for further analysis. To examine the stability of the selected models, we performed a 300 ns all-atom molecular dynamics (MD) simulation via Desmond (76). The Cα RMSD of the final selected model plateaued under ~3.5Å, supporting a stable fold and feasible intramolecular interactions (fig. S1).

Peptide Docking

The N-terminal peptide of XCL1 (Residues 1–10; N-[Val-Gly-Ser-Glu-Val-Ser-Asp-Lys-Arg-Thr]-C) was docked into the homology model of XCR1 generated above using Rosetta's FlexPepDock *ab-initio* protocol (46, 77, 78), similar to what has been previously published (79). As the orthosteric pocket of the Rosetta-generated homology model of XCR1 was largely inaccessible to ligand, three unique "open-pocket" poses of XCR1 were randomly selected by visual inspection for docking from the 300-ns molecular dynamic simulation trajectory (i.e., three frames from the 1000 frame trajectory; specifically frame 99, frame 475, and frame 957). The peptide was manually built in PyMol and placed away from the receptor in an extended conformation. 100,000 docked models were generated with FlexPepDock *ab-initio* and were subsequently filtered according to their relative position to

the orthosteric pocket (i.e., distance from CH2 of $Trp^{2.60}$ to CA of Val^{1} of XCL1 < 10 Å) and the energy score contributed by residue Glu^{4} of the N-terminal peptide from XCL1 (i.e., negative energy contribution). The resulting models were clustered using Calibur (80), and a representative model from the largest cluster was selected for further refinement. The selected model for each initial XCR1 pose (3 models in total) was used to seed the generation of an additional 100,000 models with FlexPepDock *ab initio*. The 100,000 newly-generated models were subjected to the filtering procedure described above, and top scoring 100 models were selected for visual inspection. The top 100 scoring poses were also analyzed for their molecular contacts using an in-house R script, using the cmap function in Bio3d (81) and a 3 Å cutoff to define intermolecular distances. Finally, 10 models were chosen by a visual inspection process comprising the selection of models in which the XCL1 N-terminal peptide sampled a variety of conformations within the orthosteric pocket. The chosen 10 models were subjected to a computational alanine scan (48) using the Robetta Computational Interface Alanine Scanning Server (47, 48) and the in silico results were compared to the experimental alanine scan results presented within to select a single final model.

Molecular Dynamics Simulations

Selected XCR1-$XCL1^{\text{N-terminal peptide}}$ models were prepared for simulation by first positioning the membrane using the PPM Server of the Orientations of Proteins in Membranes (OPM) database (82) and subsequently using the *Protein Preparation Wizard* of Maestro (Schrödinger) to cap the N- and C-terminus of the receptor and to perform H-bond optimization and protein minimization of the complex (83). Histidine residues were simulated in the neutral state (N_{ε} tautomer, HIE) and all glutamate and aspartate residues were simulated in the charged state, following several recent studies of GPCR systems (84–86). The *System Builder* in Maestro (Schrödinger) was then used to insert the prepared system into an equilibrated POPC (1-palmitoyl-2-oleoyl-sn-glycero-3-phosphocholine) bilayer according to the PPM positioning described above. Sodium and chloride ions were added to neutralize the system and reach a final NaCl concentration of 150mM. The *viparr* and *build_constraints* utilities of Desmond were used to adjust the force field parameters to utilize the CHARMM 36 force field and the TIP3P water model (87). The system was equilibrated at 310K using the *relax_membrane.py* utility of Desmond. Four 1 μs molecular dynamics simulations were subsequently performed with randomized starting velocities, each with a 300 ps recording interval and a 2 fs timestep, at 310K and 1 bar in the NPT ensemble using a Nose-Hoover thermostat and a Martyna-Tobias-Klein barostat with a 2.0 picosecond relaxation time. The resulting trajectory was analyzed using Visual Molecular Dynamics (VMD) (88) and the R package Bio3D (81). Note that in Figs. 4–6 and fig. S3, a single representative simulation is shown for clarity. The representative simulation corresponds to “simulation 2” as represented in fig. S2.

Nonlinear Regression and Statistical Analysis

All data are expressed as mean ± SEM. Non-linear regression was performed in Prism version 7.0c & version 8 (GraphPad Software) for ^{125}I-XCL1 CC3 radio-ligand displacement, IP_3 accumulation, and calcium flux assays. A sigmoidal dose-response (variable slope) equation with a least squares regression was used to fit all the data. Values

for the bottom and upper asymptote, LogEC50, and Hill slope were all fit, except when indicated as constrained. Values were constrained under certain instances to fit the available data points. To account for statistical differences in the data, one-way ANOVA testing was used to compare the mean LogEC50 and SEM for each XCL1 construct. Multiple comparisons were made using Dunnett's post hoc testing. Mean chemotaxis data for each XCL1 construct was statistically analyzed using multiple t test, and multiple comparisons were made using the Holm-Sidak method. A p-value of ≤ 0.05 is considered statistically significant.

Supplementary Material

Refer to Web version on PubMed Central for supplementary material.

Acknowledgments:

We thank Maibritt Sigvardt Baggesen (University of Copenhagen) for assistance with XCR1 binding and IP_3 accumulation assays; Dr. Joseph Hedrick (Schering-Plough Research Institute) for generously providing XCR1 expressing HEK293 cells; and Dr. Anthony G. Getschman (Medical College of Wisconsin) for fruitful discussion and assistance with manuscript editing.

Funding: This work was supported in part by National Institutes of Health Grants R01 AI058072 (to B.F.V.), F30 HL134253 (to M.A.T.), and F30 CA236182 (to A.F.D). M.A.T. and A.F.D. are members of the NIH supported (T32 GM080202) Medical Scientist Training Program at the Medical College of Wisconsin (MCW).

References and Notes:

1. Lei Y, Ripen AM, Ishimaru N, Ohigashi I, Nagasawa T, Jeker LT, Bosl MR, Hollander GA, Hayashi Y, Malefyt Rde W, Nitta T, Takahama Y. Aire-dependent production of XCL1 mediates medullary accumulation of thymic dendritic cells and contributes to regulatory T cell development. J Exp Med. 2011;208(2):383–94. Epub 2011/02/09. doi: 10.1084/jem.20102327. [PubMed: 21300913]
2. Ohta T, Sugiyama M, Hemmi H, Yamazaki C, Okura S, Sasaki I, Fukuda Y, Orimo T, Ishii KJ, Hoshino K, Ginhoux F, Kaisho T. Crucial roles of XCR1-expressing dendritic cells and the XCR1-XCL1 chemokine axis in intestinal immune homeostasis. Sci Rep. 2016;6:23505. doi: 10.1038/srep23505. [PubMed: 27005831]
3. Terhorst D, Fossum E, Baranska A, Tamoutounour S, Malosse C, Garbani M, Braun R, Lechat E, Crameri R, Bogen B, Henri S, Malissen B. Laser-assisted intradermal delivery of adjuvant-free vaccines targeting XCR1+ dendritic cells induces potent antitumoral responses. J Immunol. 2015;194(12):5895–902. doi: 10.4049/jimmunol.1500564. [PubMed: 25941327]
4. Rousseau RF, Haight AE, Hirschmann-Jax C, Yvon ES, Rill DR, Mei Z, Smith SC, Inman S, Cooper K, Alcoser P, Grilley B, Gee A, Popek E, Davidoff A, Bowman LC, Brenner MK, Strother D. Local and systemic effects of an allogeneic tumor cell vaccine combining transgenic human lymphotactin with interleukin-2 in patients with advanced or refractory neuroblastoma. Blood. 2003;101(5):1718–26. [PubMed: 12406881]
5. Cao X, Zhang W, He L, Xie Z, Ma S, Tao Q, Yu Y, Hamada H, Wang J. Lymphotactin gene-modified bone marrow dendritic cells act as more potent adjuvants for peptide delivery to induce specific antitumor immunity. J Immunol. 1998;161(11):6238–44. [PubMed: 9834111]
6. Sheng XL, Zhang H. In-vitro activation of cytotoxic T lymphocytes by fusion of mouse hepatocellular carcinoma cells and lymphotactin gene-modified dendritic cells. World J Gastroenterol. 2007;13(44):5944–50. [PubMed: 17990361]
7. Xia DJ, Zhang WP, Zheng S, Wang J, Pan JP, Wang Q, Zhang LH, Hamada H, Cao X. Lymphotactin cotransfection enhances the therapeutic efficacy of dendritic cells genetically modified with melanoma antigen gp100. Gene Ther. 2002;9(9):592–601. doi: 10.1038/sj.gt.3301694. [PubMed: 11973635]

8. Zhang W, He L, Yuan Z, Xie Z, Wang J, Hamada H, Cao X. Enhanced therapeutic efficacy of tumor RNA-pulsed dendritic cells after genetic modification with lymphotactin. Hum Gene Ther. 1999;10(7):1151–61. doi: 10.1089/10430349950018148. [PubMed: 10340547]
9. Cairns CM, Gordon JR, Li F, Baca-Estrada ME, Moyana T, Xiang J. Lymphotactin expression by engineered myeloma cells drives tumor regression: mediation by CD4+ and CD8+ T cells and neutrophils expressing XCR1 receptor. J Immunol. 2001;167(1):57–65. [PubMed: 11418632]
10. Russell HV, Strother D, Mei Z, Rill D, Popek E, Biagi E, Yvon E, Brenner M, Rousseau R. Phase I trial of vaccination with autologous neuroblastoma tumor cells genetically modified to secrete IL-2 and lymphotactin. J Immunother. 2007;30(2):227–33. doi: 10.1097/01.cji.0000211335.14385.57. [PubMed: 17471169]
11. Emtage PC, Wan Y, Hitt M, Graham FL, Muller WJ, Zlotnik A, Gauldie J. Adenoviral vectors expressing lymphotactin and interleukin 2 or lymphotactin and interleukin 12 synergize to facilitate tumor regression in murine breast cancer models. Hum Gene Ther. 1999;10(5):697–709. doi: 10.1089/10430349950018463. [PubMed: 10210138]
12. Ju DW, Tao Q, Cheng DS, Zhang W, Zhang M, Hamada H, Cao X. Adenovirus-mediated lymphotactin gene transfer improves therapeutic efficacy of cytosine deaminase suicide gene therapy in established murine colon carcinoma. Gene Ther. 2000;7(4):329–38. doi: 10.1038/sj.gt.3301082. [PubMed: 10694814]
13. Lazennec G, Richmond A. Chemokines and chemokine receptors: new insights into cancer-related inflammation. Trends Mol Med. 2010;16(3):133–44. doi: 10.1016/j.molmed.2010.01.003. [PubMed: 20163989]
14. Dranoff G Cytokines in cancer pathogenesis and cancer therapy. Nature reviews Cancer. 2004;4(1):11–22. doi: 10.1038/nrc1252. [PubMed: 14708024]
15. Chow MT, Luster AD. Chemokines in cancer. Cancer immunology research. 2014;2(12):1125–31. doi: 10.1158/2326-6066.CIR-14-0160. [PubMed: 25480554]
16. Mukaida N, Sasaki S, Baba T. Chemokines in cancer development and progression and their potential as targeting molecules for cancer treatment. Mediators Inflamm. 2014;2014:170381. doi: 10.1155/2014/170381. [PubMed: 24966464]
17. Keen JC, Garrett-Mayer E, Pettit C, Mack KM, Manning J, Herman JG, Davidson NE. Epigenetic regulation of protein phosphatase 2A (PP2A), lymphotactin (XCL1) and estrogen receptor alpha (ER) expression in human breast cancer cells. Cancer Biol Ther. 2004;3(12):1304–12. [PubMed: 15662126]
18. Clark-Lewis I, Dewald B, Geiser T, Moser B, Baggiolini M. Platelet factor 4 binds to interleukin 8 receptors and activates neutrophils when its N terminus is modified with Glu-Leu-Arg. Proc Natl Acad Sci U S A. 1993;90(8):3574–7. [PubMed: 8475106]
19. Crump MP, Gong JH, Loetscher P, Rajarathnam K, Amara A, Arenzana-Seisdedos F, Virelizier JL, Baggiolini M, Sykes BD, Clark-Lewis I. Solution structure and basis for functional activity of stromal cell-derived factor-1; dissociation of CXCR4 activation from binding and inhibition of HIV-1. Embo J. 1997;16(23):6996–7007. Epub 1998/01/31. doi: 10.1093/emboj/16.23.6996. [PubMed: 9384579]
20. Crump MP, Gong JH, Loetscher P, Rajarathnam K, Amara A, Arenzana-Seisdedos F, Virelizier JL, Baggiolini M, Sykes BD, Clark-Lewis I. Solution structure and basis for functional activity of stromal cell-derived factor-1; dissociation of CXCR4 activation from binding and inhibition of HIV-1. Embo J. 1997;16(23):6996–7007. doi: 10.1093/emboj/16.23.6996. [PubMed: 9384579]
21. Rajagopalan L, Rajarathnam K. Structural basis of chemokine receptor function--a model for binding affinity and ligand selectivity. Bioscience reports. 2006;26(5):325–39. Epub 2006/10/07. doi: 10.1007/s10540-006-9025-9. [PubMed: 17024562]
22. Thiele S, Steen A, Jensen PC, Mokrosinski J, Frimurer TM, Rosenkilde MM. Allosteric and orthosteric sites in CC chemokine receptor (CCR5), a chimeric receptor approach. J Biol Chem. 2011;286(43):37543–54. doi: 10.1074/jbc.M111.243808. [PubMed: 21878623]
23. Ferguson SS. Evolving concepts in G protein-coupled receptor endocytosis: the role in receptor desensitization and signaling. Pharmacol Rev. 2001;53(1):1–24. [PubMed: 11171937]

24. Kunz M, Ibrahim SM. Cytokines and cytokine profiles in human autoimmune diseases and animal models of autoimmunity. Mediators Inflamm. 2009;2009:979258. doi: 10.1155/2009/979258. [PubMed: 19884985]
25. Gelmini S, Mangoni M, Serio M, Romagnani P, Lazzeri E. The critical role of SDF-1/CXCR4 axis in cancer and cancer stem cells metastasis. J Endocrinol Invest. 2008;31(9):809–19. doi: 10.1007/BF03349262. [PubMed: 18997494]
26. Kuloglu ES, McCaslin DR, Kitabwalla M, Pauza CD, Markley JL, Volkman BF. Monomeric solution structure of the prototypical 'C' chemokine lymphotactin. Biochemistry. 2001;40(42):12486–96. [PubMed: 11601972]
27. Kuloglu ES, McCaslin DR, Markley JL, Volkman BF. Structural rearrangement of human lymphotactin, a C chemokine, under physiological solution conditions. J Biol Chem. 2002;277(20):17863–70. Epub 2002/03/13. doi: 10.1074/jbc.M200402200. [PubMed: 11889129]
28. Tuinstra RL, Peterson FC, Kutlesa S, Elgin ES, Kron MA, Volkman BF. Interconversion between two unrelated protein folds in the lymphotactin native state. Proc Natl Acad Sci U S A. 2008;105(13):5057–62. Epub 2008/03/28. doi: 10.1073/pnas.0709518105. [PubMed: 18364395]
29. Tuinstra RL, Peterson FC, Elgin ES, Pelzek AJ, Volkman BF. An engineered second disulfide bond restricts lymphotactin/XCL1 to a chemokine-like conformation with XCR1 agonist activity. Biochemistry. 2007;46(10):2564–73. Epub 2007/02/17. doi: 10.1021/bi602365d. [PubMed: 17302442]
30. Murzin AG. Biochemistry. Metamorphic proteins. Science. 2008;320(5884):1725–6. [PubMed: 18583598]
31. Guzzo C, Fox J, Lin Y, Miao H, Cimbro R, Volkman BF, Fauci AS, Lusso P. The CD8-derived chemokine XCL1/lymphotactin is a conformation-dependent, broad-spectrum inhibitor of HIV-1. PLoS Pathog. 2013;9(12):e1003852 Epub 2014/01/05. doi: 10.1371/journal.ppat.1003852. [PubMed: 24385911]
32. Fox JC, Tyler RC, Guzzo C, Tuinstra RL, Peterson FC, Lusso P, Volkman BF. Engineering Metamorphic Chemokine Lymphotactin/XCL1 into the GAG-Binding, HIV-Inhibitory Dimer Conformation. ACS Chem Biol. 2015;10(11):2580–8. Epub 2015/08/25. doi: 10.1021/acschembio.5b00542. [PubMed: 26302421]
33. Guzzo C, Fox JC, Miao H, Volkman BF, Lusso P. Structural Determinants for the Selective Anti-HIV-1 Activity of the All-beta Alternative Conformer of XCL1. J Virol. 2015;17:9061–7. Epub 2015/06/19. doi: 10.1128/JVI.01285-15.
34. Fox JC, Tyler RC, Peterson FC, Dyer DP, Zhang F, Linhardt RJ, Handel TM, Volkman BF. Examination of Glycosaminoglycan Binding Sites on the XCL1 Dimer. Biochemistry 2016;55(8):1214–25. Epub 2016/02/03. doi: 10.1021/acs.biochem.5b01329. [PubMed: 26836755]
35. Matsuo K, Kitahata K, Kawabata F, Kamei M, Hara Y, Takamura S, Oiso N, Kawada A, Yoshie O, Nakayama T. A Highly Active Form of XCL1/Lymphotactin Functions as an Effective Adjuvant to Recruit Cross-Presenting Dendritic Cells for Induction of Effector and Memory CD8(+) T Cells. Front Immunol. 2018;9:2775. doi: 10.3389/fimmu.2018.02775. [PubMed: 30542351]
36. Luttichau HR. The cytomegalovirus UL146 gene product vCXCL1 targets both CXCR1 and CXCR2 as an agonist. J Biol Chem. 2010;285(12):9137–46. doi: 10.1074/jbc.M109.002774. [PubMed: 20044480]
37. Jensen PC, Thiele S, Ulven T, Schwartz TW, Rosenkilde MM. Positive versus negative modulation of different endogenous chemokines for CC-chemokine receptor 1 by small molecule agonists through allosteric versus orthosteric binding. J Biol Chem. 2008;283(34):23121–8. doi: 10.1074/jbc.M803458200. [PubMed: 18559339]
38. Neptune ER, Bourne HR. Receptors induce chemotaxis by releasing the betagamma subunit of Gi, not by activating Gq or Gs. Proc Natl Acad Sci U S A. 1997;94(26):14489–94. [PubMed: 9405640]
39. Gilman AG. G proteins: transducers of receptor-generated signals. Annu Rev Biochem. 1987;56:615–49. doi: 10.1146/annurev.bi.56.070187.003151. [PubMed: 3113327]
40. Thomsen W, Frazer J, Unett D. Functional assays for screening GPCR targets. Current opinion in biotechnology. 2005;16(6):655–65. doi: 10.1016/j.copbio.2005.10.008. [PubMed: 16257523]

41. Toetsch S, Olwell P, Prina-Mello A, Volkov Y. The evolution of chemotaxis assays from static models to physiologically relevant platforms. Integrative biology : quantitative biosciences from nano to macro. 2009;1(2):170–81. doi: 10.1039/b814567a. [PubMed: 20023801]

42. Calabrese EJ. Cell migration/chemotaxis: biphasic dose responses. Crit Rev Toxicol. 2001;31(4–5): 615–24. Epub 2001/08/16. doi: 10.1080/20014091111875. [PubMed: 11504186]

43. Kufareva I, Salanga CL, Handel TM. Chemokine and chemokine receptor structure and interactions: implications for therapeutic strategies. Immunol Cell Biol. 2015;93(4):372–83. doi: 10.1038/icb.2015.15. [PubMed: 25708536]

44. Bender BJ, Cisneros A 3rd, Duran AM, Finn JA, Fu D, Lokits AD, Mueller BK, Sangha AK, Sauer MF, Sevy AM, Sliwoski G, Sheehan JH, DiMaio F, Meiler J, Moretti R. Protocols for Molecular Modeling with Rosetta3 and RosettaScripts. Biochemistry. 2016;55(34):4748–63. doi: 10.1021/acs.biochem.6b00444. [PubMed: 27490953]

45. Song Y, DiMaio F, Wang RY, Kim D, Miles C, Brunette T, Thompson J, Baker D. High-resolution comparative modeling with RosettaCM. Structure. 2013;21(10):1735–42. doi: 10.1016/j.str.2013.08.005. [PubMed: 24035711]

46. Raveh B, London N, Zimmerman L, Schueler-Furman O. Rosetta FlexPepDock ab-initio: simultaneous folding, docking and refinement of peptides onto their receptors. PLoS One. 2011;6(4):e18934. doi: 10.1371/journal.pone.0018934. [PubMed: 21572516]

47. Kortemme T, Baker D. A simple physical model for binding energy hot spots in protein-protein complexes. Proc Natl Acad Sci U S A. 2002;99(22):14116–21. doi: 10.1073/pnas.202485799. [PubMed: 12381794]

48. Kortemme T, Kim DE, Baker D. Computational alanine scanning of protein-protein interfaces. Sci STKE. 2004;2004(219):pl2. doi: 10.1126/stke.2192004pl2. [PubMed: 14872095]

49. Nomiyama H, Yoshie O. Functional roles of evolutionary conserved motifs and residues in vertebrate chemokine receptors. J Leukoc Biol. 2015;97(1):39–47. doi: 10.1189/jlb.2RU0614-290R. [PubMed: 25416815]

50. Arimont M, Sun SL, Leurs R, Smit M, de Esch IJP, de Graaf C. Structural Analysis of Chemokine Receptor-Ligand Interactions. J Med Chem. 2017;60(12):4735–79. doi: 10.1021/acs.jmedchem.6b01309. [PubMed: 28165741]

51. Rosenkilde MM, Schwartz TW. GluVII:06--a highly conserved and selective anchor point for non-peptide ligands in chemokine receptors. Curr Top Med Chem. 2006;6(13):1319–33. [PubMed: 16918451]

52. Scholten DJ, Canals M, Maussang D, Roumen L, Smit MJ, Wijtmans M, de Graaf C, Vischer HF, Leurs R. Pharmacological modulation of chemokine receptor function. Br J Pharmacol. 2012;165(6):1617–43. doi: 10.1111/j.1476-5381.2011.01551.x. [PubMed: 21699506]

53. Qin L, Kufareva I, Holden LG, Wang C, Zheng Y, Zhao C, Fenalti G, Wu H, Han GW, Cherezov V, Abagyan R, Stevens RC, Handel TM. Structural biology. Crystal structure of the chemokine receptor CXCR4 in complex with a viral chemokine. Science. 2015;347(6226):1117–22. doi: 10.1126/science.1261064. [PubMed: 25612609]

54. Burg JS, Ingram JR, Venkatakrishnan AJ, Jude KM, Dukkipati A, Feinberg EN, Angelini A, Waghray D, Dror RO, Ploegh HL, Garcia KC. Structural biology. Structural basis for chemokine recognition and activation of a viral G protein-coupled receptor. Science. 2015;347(6226):1113–7. doi: 10.1126/science.aaa5026. [PubMed: 25745166]

55. Zheng Y, Han GW, Abagyan R, Wu B, Stevens RC, Cherezov V, Kufareva I, Handel TM. Structure of CC Chemokine Receptor 5 with a Potent Chemokine Antagonist Reveals Mechanisms of Chemokine Recognition and Molecular Mimicry by HIV. Immunity. 2017;46(6):1005–17 e5. doi: 10.1016/j.immuni.2017.05.002. [PubMed: 28636951]

56. Pakianathan DR, Kuta EG, Artis DR, Skelton NJ, Hebert CA. Distinct but overlapping epitopes for the interaction of a CC-chemokine with CCR1, CCR3 and CCR5. Biochemistry. 1997;36(32): 9642–8. doi: 10.1021/bi970593z. [PubMed: 9289016]

57. Hebert CA, Vitangcol RV, Baker JB. Scanning mutagenesis of interleukin-8 identifies a cluster of residues required for receptor binding. J Biol Chem. 1991;266(28):18989–94. [PubMed: 1918013]

58. Ohnishi Y, Senda T, Nandhagopal N, Sugimoto K, Shioda T, Nagal Y, Mitsui Y. Crystal structure of recombinant native SDF-1alpha with additional mutagenesis studies: an attempt at a more

comprehensive interpretation of accumulated structure-activity relationship data. J Interferon Cytokine Res. 2000;20(8):691–700. doi: 10.1089/10799900050116390. [PubMed: 10954912]

59. Strieter RM, Polverini PJ, Kunkel SL, Arenberg DA, Burdick MD, Kasper J, Dzuiba J, Van Damme J, Walz A, Marriott D, et al. The functional role of the ELR motif in CXC chemokine-mediated angiogenesis. J Biol Chem. 1995;270(45):27348–57. [PubMed: 7592998]
60. Laurence JS, LiWang AC, LiWang PJ. Effect of N-terminal truncation and solution conditions on chemokine dimer stability: nuclear magnetic resonance structural analysis of macrophage inflammatory protein 1 beta mutants. Biochemistry. 1998;37(26):9346–54. doi: 10.1021/bi980329l. [PubMed: 9649315]
61. Chan HCS, Li Y, Dahoun T, Vogel H, Yuan S. New Binding Sites, New Opportunities for GPCR Drug Discovery. Trends in biochemical sciences. 2019;44(4):312–30. doi: 10.1016/j.tibs.2018.11.011. [PubMed: 30612897]
62. Ahuja S, Smith SO. Multiple switches in G protein-coupled receptor activation. Trends Pharmacol Sci. 2009;30(9):494–502. doi: 10.1016/j.tips.2009.06.003. [PubMed: 19732972]
63. Kimura KT, Asada H, Inoue A, Kadji FMN, Im D, Mori C, Arakawa T, Hirata K, Nomura Y, Nomura N, Aoki J, Iwata S, Shimamura T. Structures of the 5-HT2A receptor in complex with the antipsychotics risperidone and zotepine. Nature structural & molecular biology. 2019;26(2):121–8. doi: 10.1038/s41594-018-0180-z.
64. Lecture Course: NMR Spectroscopy:1–142.
65. Kroczek AL, Hartung E, Gurka S, Becker M, Reeg N, Mages HW, Voigt S, Freund C, Kroczek RA. Structure-Function Relationship of XCL1 Used for in vivo Targeting of Antigen Into XCR1(+) Dendritic Cells. Front Immunol. 2018;9:2806. doi: 10.3389/fimmu.2018.02806. [PubMed: 30619244]
66. Fox JC, Nakayama T, Tyler RC, Sander TL, Yoshie O, Volkman BF. Structural and agonist properties of XCL2, the other member of the C-chemokine subfamily. Cytokine. 2015;71(2):302–11. Epub 2014/12/17. doi: 10.1016/j.cyto.2014.11.010. [PubMed: 25497737]
67. Getschman AE, Imai Y, Larsen O, Peterson FC, Wu X, Rosenkilde MM, Hwang ST, Volkman BF. Protein engineering of the chemokine CCL20 prevents psoriasiform dermatitis in an IL-23-dependent murine model. Proc Natl Acad Sci U S A. 2017;114(47):12460–5. doi: 10.1073/pnas.1704958114. [PubMed: 29109267]
68. Rosenkilde MM, Gerlach LO, Hatse S, Skerlj RT, Schols D, Bridger GJ, Schwartz TW. Molecular mechanism of action of monocyclam versus bicyclam non-peptide antagonists in the CXCR4 chemokine receptor. J Biol Chem. 2007;282(37):27354–65. doi: 10.1074/jbc.M704739200. [PubMed: 17599916]
69. Shan L, Qiao X, Oldham E, Catron D, Kaminski H, Lundell D, Zlotnik A, Gustafson E, Hedrick JA. Identification of viral macrophage inflammatory protein (vMIP)-II as a ligand for GPR5/XCR1. Biochem Biophys Res Commun. 2000;268(3):938–41. Epub 2000/02/19. doi: 10.1006/bbrc.2000.2235. [PubMed: 10679309]
70. Yoshida T, Imai T, Kakizaki M, Nishimura M, Takagi S, Yoshie O. Identification of single C motif-1/lymphotactin receptor XCR1. J Biol Chem. 1998;273(26):16551–4. [PubMed: 9632725]
71. The UniProt C UniProt: the universal protein knowledgebase. Nucleic Acids Res. 2017;45(D1):D158–D69. doi: 10.1093/nar/gkw1099. [PubMed: 27899622]
72. Sievers F, Wilm A, Dineen D, Gibson TJ, Karplus K, Li W, Lopez R, McWilliam H, Remmert M, Soding J, Thompson JD, Higgins DG. Fast, scalable generation of high-quality protein multiple sequence alignments using Clustal Omega. Mol Syst Biol. 2011;7:539. doi: 10.1038/msb.2011.75. [PubMed: 21988835]
73. Kim DE, Chivian D, Baker D. Protein structure prediction and analysis using the Robetta server. Nucleic Acids Res. 2004;32(Web Server issue):W526–31. doi: 10.1093/nar/gkh468. [PubMed: 15215442]
74. Viklund H, Elofsson A. OCTOPUS: improving topology prediction by two-track ANN-based preference scores and an extended topological grammar. Bioinformatics. 2008;24(15):1662–8. doi: 10.1093/bioinformatics/btn221. [PubMed: 18474507]

75. Tyka MD, Keedy DA, Andre I, Dimaio F, Song Y, Richardson DC, Richardson JS, Baker D. Alternate states of proteins revealed by detailed energy landscape mapping. J Mol Biol. 2011;405(2):607–18. doi: 10.1016/j.jmb.2010.11.008. [PubMed: 21073878]
76. Bowers KJ, Chow E, Xu H, Dror RO, Eastwood MP, Gregersen BA, Klepeis JL, Kolossvary I, Moraes MA, Sacerdoti FD, Salmon JK, Shan Y, Shaw DE. Scalable Algorithms for Molecular Dynamics Simulations on Commodity Clusters. IEEE transactions on biomedical circuits and systems. 2006:43-. doi: 10.1109/SC.2006.54.
77. Alam N, Schueler-Furman O. Modeling Peptide-Protein Structure and Binding Using Monte Carlo Sampling Approaches: Rosetta FlexPepDock and FlexPepBind. Methods Mol Biol. 2017;1561:139–69. doi: 10.1007/978-1-4939-6798-8_9. [PubMed: 28236237]
78. Raveh B, London N, Schueler-Furman O. Sub-angstrom modeling of complexes between flexible peptides and globular proteins. Proteins. 2010;78(9):2029–40. doi: 10.1002/prot.22716. [PubMed: 20455260]
79. Ziarek JJ, Kleist AB, London N, Raveh B, Montpas N, Bonneterre J, St-Onge G, DiCosmo-Ponticello CJ, Koplinski CA, Roy I, Stephens B, Thelen S, Veldkamp CT, Coffman FD, Cohen MC, Dwinell MB, Thelen M, Peterson FC, Heveker N, Volkman BF. Structural basis for chemokine recognition by a G protein-coupled receptor and implications for receptor activation. Sci Signal. 2017;10(471). doi: 10.1126/scisignal.aah5756.
80. Li SC, Ng YK. Calibur: a tool for clustering large numbers of protein decoys. BMC Bioinformatics. 2010;11:25. doi: 10.1186/1471-2105-11-25. [PubMed: 20070892]
81. Grant BJ, Rodrigues AP, ElSawy KM, McCammon JA, Caves LS. Bio3d: an R package for the comparative analysis of protein structures. Bioinformatics. 2006;22(21):2695–6. doi: 10.1093/bioinformatics/btl461. [PubMed: 16940322]
82. Lomize MA, Pogozheva ID, Joo H, Mosberg HI, Lomize AL. OPM database and PPM web server: resources for positioning of proteins in membranes. Nucleic Acids Res. 2012;40(Database issue):D370–6. doi: 10.1093/nar/gkr703. [PubMed: 21890895]
83. Sastry GM, Adzhigirey M, Day T, Annabhimoju R, Sherman W. Protein and ligand preparation: parameters, protocols, and influence on virtual screening enrichments. J Comput Aided Mol Des. 2013;27(3):221–34. doi: 10.1007/s10822-013-9644-8. [PubMed: 23579614]
84. Liu X, Ahn S, Kahsai AW, Meng KC, Latorraca NR, Pani B, Venkatakrishnan AJ, Masoudi A, Weis WI, Dror RO, Chen X, Lefkowitz RJ, Kobilka BK. Mechanism of intracellular allosteric beta2AR antagonist revealed by X-ray crystal structure. Nature. 2017;548(7668):480–4. doi: 10.1038/nature23652. [PubMed: 28813418]
85. Wacker D, Wang S, McCorvy JD, Betz RM, Venkatakrishnan AJ, Levit A, Lansu K, Schools ZL, Che T, Nichols DE, Shoichet BK, Dror RO, Roth BL. Crystal Structure of an LSD-Bound Human Serotonin Receptor. Cell. 2017;168(3):377–89 e12. doi: 10.1016/j.cell.2016.12.033. [PubMed: 28129538]
86. Huang W, Manglik A, Venkatakrishnan AJ, Laeremans T, Feinberg EN, Sanborn AL, Kato HE, Livingston KE, Thorsen TS, Kling RC, Granier S, Gmeiner P, Husbands SM, Traynor JR, Weis WI, Steyaert J, Dror RO, Kobilka BK. Structural insights into micro-opioid receptor activation. Nature. 2015;524(7565):315–21. doi: 10.1038/nature14886. [PubMed: 26245379]
87. Best RB, Zhu X, Shim J, Lopes PE, Mittal J, Feig M, Mackerell AD Jr., Optimization of the additive CHARMM all-atom protein force field targeting improved sampling of the backbone phi, psi and side-chain chi(1) and chi(2) dihedral angles. J Chem Theory Comput. 2012;8(9):3257–73. doi: 10.1021/ct300400x. [PubMed: 23341755]
88. Humphrey W, Dalke A, Schulten K. VMD: visual molecular dynamics. J Mol Graph. 1996;14(1):33–8, [PubMed: 8744570]

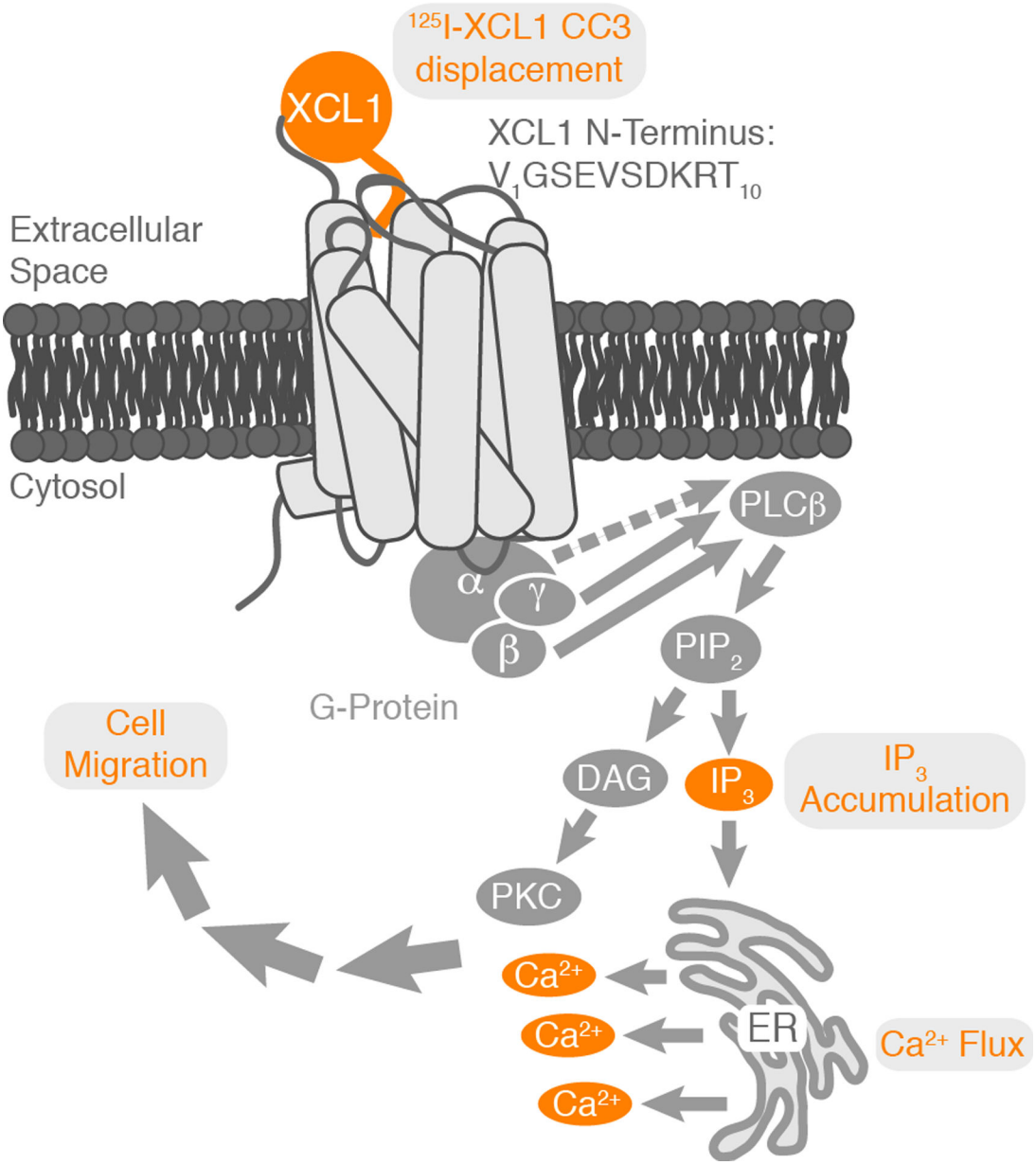

Fig. 1. Working model of XCL1 CC3-XCR1 binding and receptor activation.

This figure illustrates the typical chemokine-receptor activation through a two-site mechanism. Once activated the GPCR XCR1 activates a G protein that initiates several downstream signaling cascades. For brevity, only a few pathways are illustrated here. To pinpoint amino acids that are crucial for XCR1 activation, alanine-scanning mutagenesis was completed on the first 10 amino acids of XCL1-CC3 (V^1 to T^{10}). Each variant was then analyzed for its ability to bind and activate XCR1 and induce downstream signaling events. These signaling events, indicated by shaded gray boxes, were measured through various cellular assays.

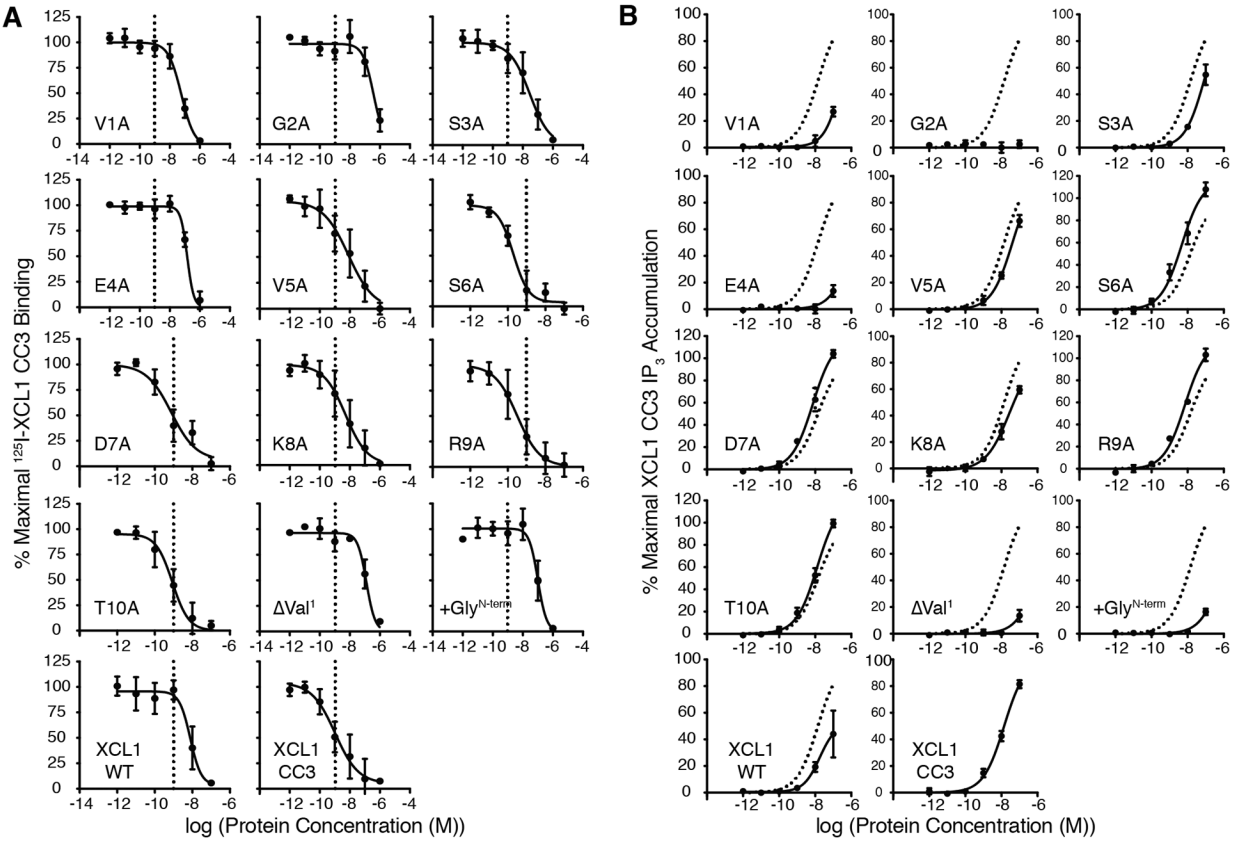

Fig. 2. ^{125}I-XCL1 CC3 displacement and ^{3}H-IP$_3$ accumulation by XCL1 N-terminal variants.

(A) XCR1 transfected COS-7 cells were incubated with ^{125}I-XCL1 CC3 along with unlabeled XCL1 ligands at concentrations indicated above for 3 hours and gamma radiation was measured ($n \geq 4$). Corresponding EC_{50} values and other fitting parameters for each ligand can be found in table S1. The dotted line indicates the EC_{50} for XCL1 CC3 = 1 nM and is added to all graphs as a point of reference. (**B**) COS-7 cells transfected with XCR1 and G_{qi4myr} were incubated with [^{3}H] myo-inositol overnight, washed, incubated with XCL1 ligands for 1.5 hours, and lysed, then scintillation was measured (n = 3 experiments). The solid lines represent ^{3}H-IP$_3$ measurement for each XCL1 ligand. The dotted curve represent ^{3}H-IP$_3$ measurement for XCL1 CC3 and are added to all other XCL1 ligand plots as a point of reference. Corresponding EC_{50} values and other fitting parameters for each ligand can be found in table S1.

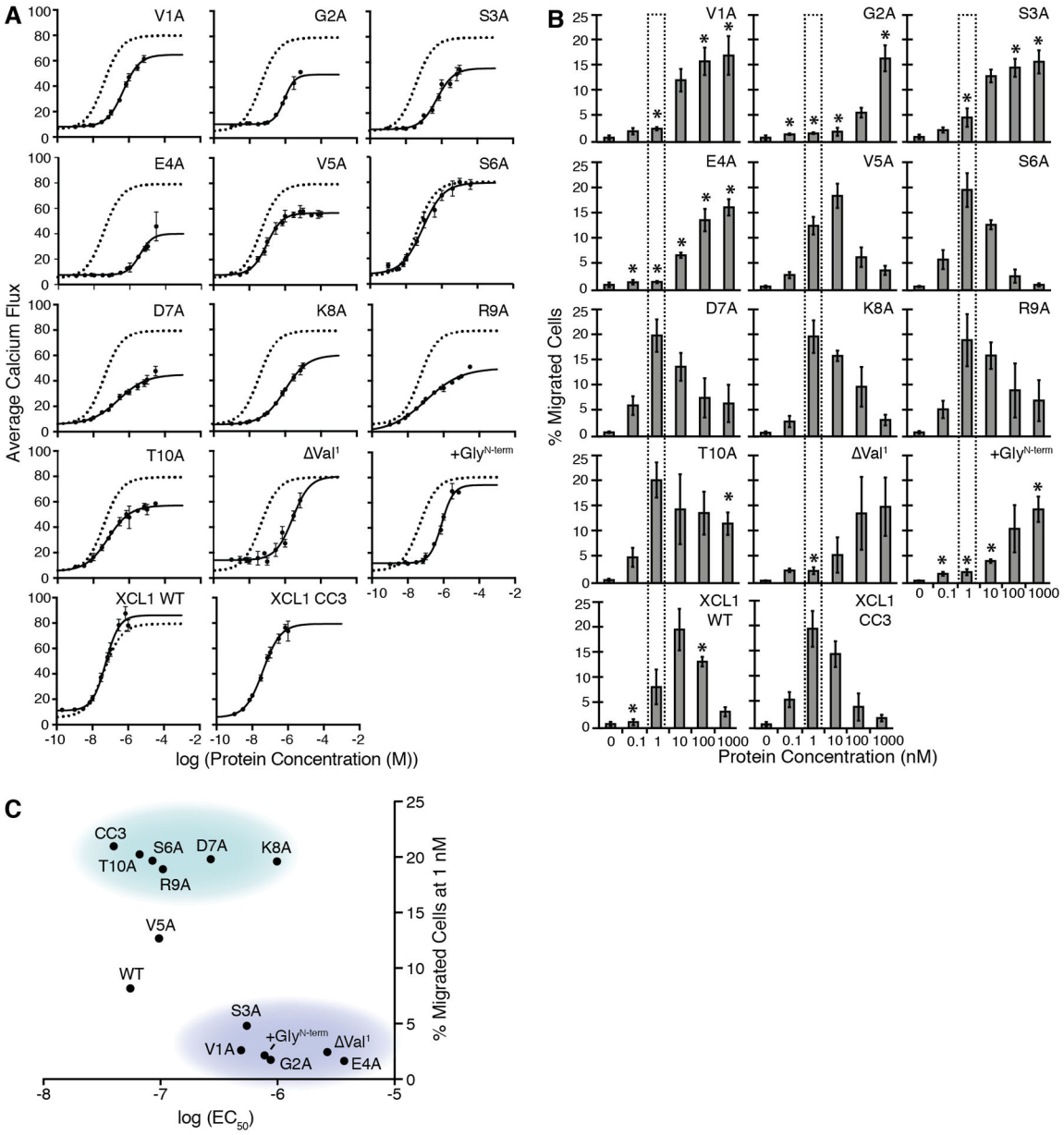

Fig. 3. Calcium flux and chemotaxis response in XCR1-expressing cells treated with XCL1 N-terminal variants.

(**A**) HEK293 cells were transfected with human XCR1 and incubated with XCL1 N-terminal variants at various concentrations. Corresponding EC_{50} values are provided in table S1. The dotted curve represent calcium flux measurement for XCL1 CC3 and are added to all other XCL1 ligand plots as a point of reference. The data are the mean ± SEM. (n ≥ 3 experiments). (**B**) Murine L1.2 cells were transfected with human XCR1 and incubated with various concentrations of XCL1 N-terminal variants in a transwell assay. The dotted box represents the maximal chemotaxis of XCL1 CC3 (1 nM) and is shown on each graph to highlight deviations in maximal chemotaxis relative to CC3. Data are mean ± SEM (n = 3 experiments). * $P<0.05$ compared with CC3, bottom right, by using the Holm-Sidak test). Maximal chemotaxis concentrations for each variant can be found in table S2. (**C**)

Correlation plot comparing log(EC_{50}) for each variant with the percent of migrated cells at 1 nM. Residues shaded in purple indicate variants with largest defect; residues shaded in cyan have XCR1-activation properties similar to those of XCL1 CC3.

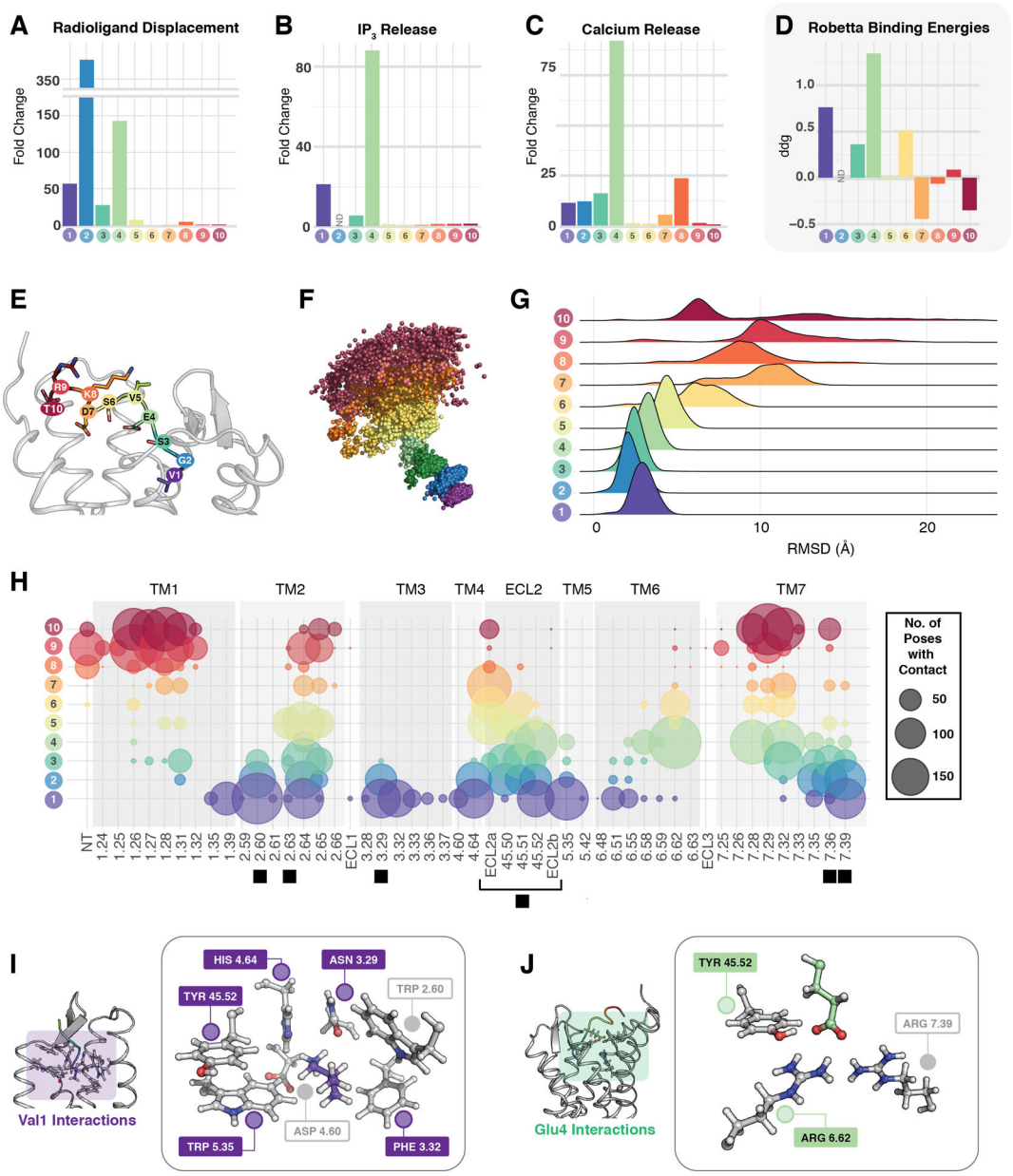

Fig. 4. Modeling of XCR1-XCL1 N-terminal interactions.

(**A to C**) Graphical representations of radioligand displacement (A), IP_3 accumulation (B), and calcium release (C) data, shown as the fold change in EC_{50} value as compared to XCL1 CC3 for each N-terminal alanine variant (labeled according to residue number, 1 to 10). Color scheme is consistent throughout the figure. Data are means of >4 experiments for radioligand displacement, 3 experiments for IP_3 release, and > 3 experiments for calcium flux. (**D**) Changes in binding energies (ddg) upon mutation of each residue in the XCL1 N-terminal peptide to an alanine using the Robetta online server. ND, no data. (**E**) The docked XCR1-$XCL1^{N\text{-terminal Peptide}}$ structure chosen for further analysis. (**F**) The Cα position of each residue of the N-terminal peptide of XCL1, colored according to residue number, over the course of a representative 1 μs molecular dynamics simulation. Residues with low Cα

RMSD distribution (more contacts with XCR1) are indicated by tightly grouped sets of spheres; residues with high Cα RMSD (less contacts with XCR1) have dispersed grouping of spheres. (**G**) Histogram representing the average Cα RMSD of each residue of the N-terminal peptide of XCL1 over the course of the representative 1 μs molecular dynamics simulation as shown in (F). (**H**) Contact network map showing contacts between the top 100 docked poses between the XCL1 N-terminal peptide (residues 1–10, y axis) and XCR1 (residues numbered according to Ballesteros-Weinstein nomenclature, x axis) for each of the three XCR1 structures docked. The size of each graphed circle represents the number of poses with the contact. TM, transmembrane. ECL, extracellular loop. Black squares beneath XCR1 residues indicate known contacts for other chemokine-chemokine receptor complexes. (**I**) Contacts between Val^1 of the XCL1 N-terminal peptide (shown in purple) and XCR1 (shown in gray). XCR1 residues are identified with their Ballesteros-Weinstein nomenclature. Purple box indicates the residue makes contact with Val^1 of XCL1. (**J**) Contacts between Glu^4 of the XCL1 N-terminal peptide (green) and XCR1 (grey). Residues making a direct contact are shown in green.

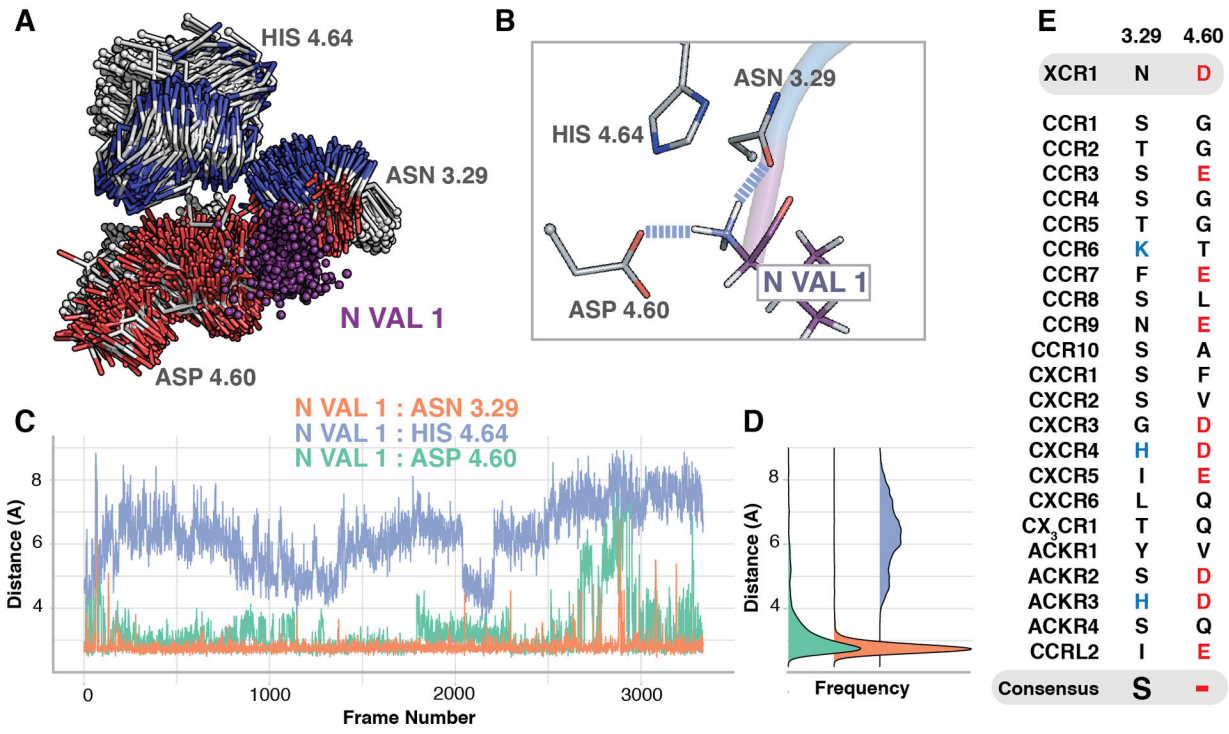

Fig. 5. MD simulation predicts key interactions between the amino terminus of XCL1 and asparagine 3.29 and aspartate 4.60

(**A**) Positions of the XCL1 N-terminal peptide amino terminus (N Val^{1}; nitrogen represented as spheres, purple) and its potential interacting partners His$^{4.64}$, Asn$^{3.29}$, and Asp$^{4.60}$ over the course of a representative 1 μs MD simulation. (**B**) The amino terminus primarily interacts with Asn$^{3.29}$ and Asp$^{4.60}$. (**C**) Distance between the nitrogen atom of the amino terminus of the XCL1 N-terminal peptide (N Val^{1}) and Asn$^{3.29}$ (OD1, orange), His$^{4.64}$ (NE2, blue), and Asp$^{4.60}$ (OD2, green) over the course of the representative 1 μs MD simulation. Distance in Angstroms. (**D**) Average frequency of interactions between the amino terminus of the XCL1 N-terminal peptide and either Asn$^{3.29}$ (OD1, orange), His$^{4.64}$ (NE2, blue), and Asp$^{4.60}$ (OD2, green) over the course of the representative 1 μs MD simulation. Distance in Angstroms. (**E**) Amino acids at position 3.29 and 4.60 in other chemokine receptors.

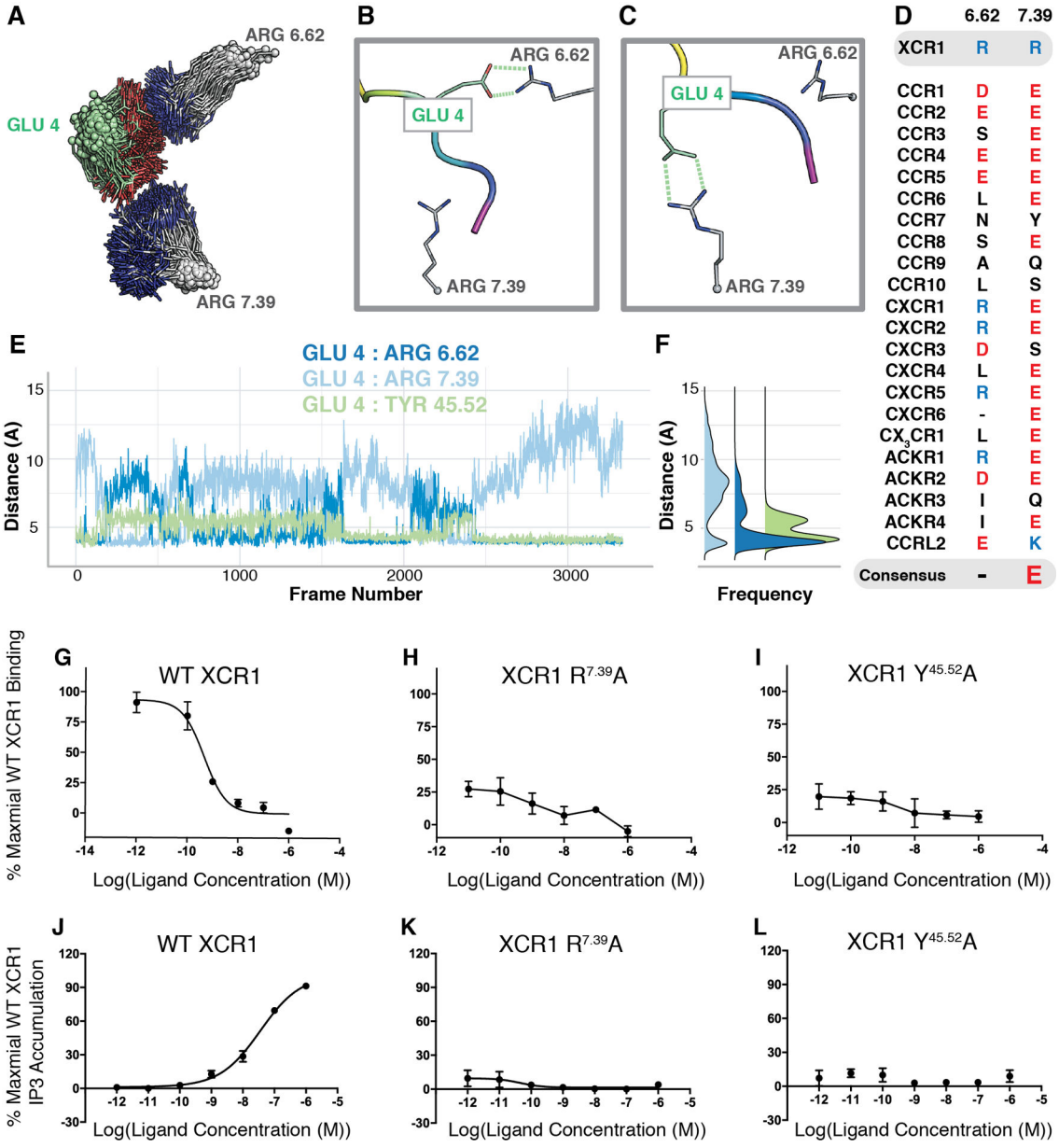

Fig. 6. Modeling and in vitro validation of key interactions between glutamate 4 of XCL1 and two arginine residues and a tyrosine residue of XCR1.

(**A**) Positions of Glu^{4} of the XCL1 N-terminal peptide and XCR1 residues $Arg^{6.62}$, $Arg^{7.39}$, and $Tyr^{45.52}$ (Ballesteros-Weinstein nomenclature) over the course of a representative 1 μs MD simulation. Cα represented as spheres. (**B**) and (**C**) Glu^{4} of the XCL1 N-terminal peptide interacts with $Arg^{6.62}$ primarily (**B**) but also interacts briefly with $Arg^{7.39}$ (**C**). (**D**) Amino acids at position 6.62 and 7.39 in other chemokine receptors. Red, negatively charged. Blue, positively charged. Black, not charged. (**E**) Distances between Glu^{4} (CD) and $Arg^{6.62}$ (CZ, dark blue), $Arg^{7.39}$ (CZ, light blue), and $Y^{45.52}$ (CZ, green) over the course of a representative 1 μs MD simulation. Distance in Angstroms. (**F**) Average frequency of interaction between Glu^{4} and $Arg^{6.62}$ (dark blue), $Arg^{7.39}$ (light blue), or $Y^{45.52}$ (green) over the course of the representative 1 μs MD simulation shown in (E). Distance in Angstroms.

(**G to L**) ^{125}I-XCL1 CC3 displacement and ^{3}H-IP_3 accumulation by XCR1 variants. XCR1 variants were designed based on computational modeling results and tested for binding (G to I) and signaling (J to L), respectively, in response to CC3. WT XCR1 (G, J) shown for reference. Data are mean ± SD from 3 experiments.